PHYSICAL REVIEW B VOLUME 54, NUMBER 12 15 SEPTEMBER 1996-II

Energy transfer, trapping, and the interaction potential in hyperthermal Na^+ scattering from Cu(001)

C. A. DiRubio,* R. L. McEachern,† J. G. McLean, and B. H. Cooper
Laboratory of Atomic and Solid State Physics, Cornell University, Ithaca, New York 14853

(Received 10 August 1995; revised manuscript received 3 May 1996)

In this paper we present measured energy and angular distributions for Na^+ scattering from Cu(001) with incident energies ranging from 10 to 100 eV. Excellent agreement with the measured spectra over the full range of incident energies is achieved with simulations using a scattering potential that consists of two parts, both of which we discuss in detail in this paper. The first is a sum of Hartree-Fock $(Na\text{-}Cu)^+$ pair potentials where the sum runs over the surface atoms nearest the scattering ion. To this we add an attractive potential that approaches the classical image potential far from the surface, but saturates close to the surface. From these spectra we extract detailed information about the scattering dynamics, such as the scattering trajectories, energy transfer to the surface, and particle trapping. For energies below 100 eV we find that the scattering is particularly sensitive to the attractive term in the potential. In particular, as the incident energy is reduced the scattered angular distributions broaden, the fractional energy transfer to the surface increases, and trapping of the ions by the surface is observed. This sensitivity enables us to put bounds on the depth of the attractive well in the potential. According to the simulations there is a minimum in the trapping probability at incident energies between 15 and 30 eV. Furthermore, they indicate that the trajectories that lead to trapping at energies below and above the minimum differ markedly, particularly in the energy transfer in the initial collision with the surface. [S0163-1829(96)02836-6]

I. INTRODUCTION

An understanding of the collision dynamics of hyperthermal energy ions (energies ranging from a few eV to a few hundred eV) with surfaces is important for many technological applications including reactive ion-beam etching and both ion-assisted and direct ion-beam deposition[1,2] of thin films. Trapping and energy transfer are among the fundamental collision processes that are important in these applications. The attractive part of the ion-surface interaction potential makes trapping possible and plays an increasingly important role in determining the energy transfer as the incident kinetic energy E_0 is reduced below 100 eV. This sensitivity to the attractive interaction begins at relatively high incident energies because the depth of the attractive well for species that chemisorb (e.g., alkalis on metals) is typically on the order of 1–3 eV. For recent reviews of scattering at hyperthermal energies see Refs. 3 and 4.

A detailed understanding of scattering dynamics at hyperthermal energies and the influence of the attractive well on these dynamics can be obtained by comparing measured ion scattering distributions to classical trajectory simulations. Alkali ion scattering from metal surfaces is an ideal model system for such studies. The noble-gas electronic structure of singly ionized alkalis simplifies the construction of the interaction potential used in the simulations and the relatively well understood charge transfer behavior simplifies the interpretation of the energy spectra.

In this paper we present a detailed study, using both experiments and simulations, of the scattering dynamics and interaction potential for hyperthermal (10–100 eV) Na^+ scattering from Cu(001). We present measured energy- and angle-resolved scattering distributions and compare them with simulations using a model potential consisting of a sum of Hartree-Fock pair potentials with an additional attractive term to account for the interaction of the ion with its induced image charge in the surface. The potential is discussed in detail in Sec. IV and in the Appendix, but we note here that the only free parameters are in the attractive term.

The simulated distributions are in excellent agreement with measurements over the entire range of incident energies. We have found that for the Na^+/Cu(001) system, both the energy and angular distributions of the scattered ions are very sensitive to the attractive interaction and that the sensitivity increases as the incident energy is decreased. In particular, as the incident energy is reduced the scattered angular distributions broaden and the fractional energy transfer to the surface increases. These changes in the scattering distributions are due to the acceleration of the ion towards the surface and the resulting trajectory bending. When the attractive interaction is not included in the scattering potential, the simulations are in poor agreement with the measured scattering distributions. Although the scattering is relatively insensitive to the details of the potential near the minimum, these results put some constraints on the depth of the attractive well in the potential. For $E_0 \leqslant 15$ eV features have been observed in the measured and simulated scattering distributions that indicate that some of the in-plane scattered ion flux is trapped in the attractive well. From the simulations, a detailed understanding of how the attractive well influences the scattering and trapping dynamics has been obtained.

The paper is organized as follows. In Sec. II we describe our apparatus and experimental technique. The simulations and the model potential are discussed in Secs. III and IV. In Sec. V we present measured energy spectra, compare them with simulations, and then use the simulations to identify the trajectories that correspond to the peaks in the spectra. The

0163-1829/96/54(12)/8862(20)/$10.00

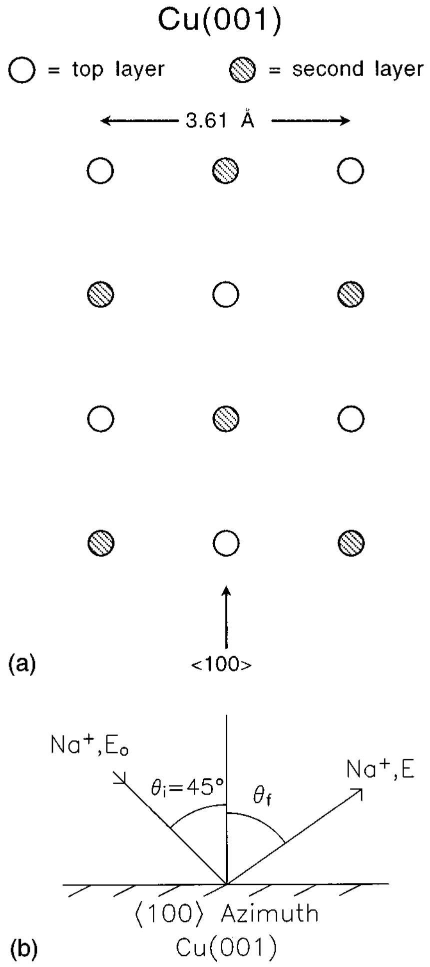

FIG. 1. (a) Schematic top view of the first and second layers of the Cu(001) surface. The spacing between the atomic planes is 1.805 Å. (b) Scattering geometry. The incident Na^+ beam is scattered along the ⟨100⟩ azimuth at $\theta_i = 45°$ for incident energies E_0 ranging from 10 to 100 eV. The in-plane scattered flux is energy analyzed as a function of final angle (θ_f).

quality of the model for the interaction potential and the importance of the attractive well are demonstrated in Sec. VI, where the measured energy and angular distributions are compared with simulations for a range of incident energies. In Sec. VII the results are discussed in more detail and in Sec. VIII the results are summarized. The repulsive term in the potential is discussed in detail in the Appendix.

II. EXPERIMENTAL TECHNIQUES

The beam line and apparatus have been described in detail elsewhere,[5–7] so we will mention only the important details here. In these experiments Na^+ with incident energies ranging from 10 to 100 eV has been scattered from a Cu(001) surface along the ⟨100⟩ azimuth at an incident angle of 45° from the surface normal (see Fig. 1). The in-plane scattered Na^+ flux is energy analyzed at final angles θ_f ranging from 6° to 90° from the surface normal [see Fig. 1(b)]. Scattering angles closer to 180° backscattering cannot be accessed due to geometrical constraints in the chamber.

The beam line is capable of transporting well-collimated, mass-selected, monoenergetic ion beams to the sample position with incident energies ranging from 5 eV to 10 keV. The source has an inherent energy spread of <0.3 eV full width at half maximum (FWHM). Typical beam characteristics at 100 eV are a 0.7 nA beam current in a 1-mm (FWHM) spot with a half-angular divergence of $<0.6°$. At 10 eV beam currents of 0.15 nA in a 2-mm spot are typical.

The scattered ion flux is energy analyzed using a hemispherical electrostatic analyzer with an energy resolution $\Delta E/E$ of 0.016 and an effective angular acceptance of $\leqslant \pm 0.5°$. After passing through the exit aperture of the analyzer, the ions are accelerated by 2400 V into a channeltron operated in pulse counting mode. This analyzer is also used to measure the incident beam energy. The accuracy of the energy measurements is limited by the uncertainty in the contact potential differences between the ion source, the sample, and the detector. We estimate that these contact potential differences result in uncertainties in the measured energies of less than ± 0.5 eV. This estimation is based on measurements of the beam energy by several different methods. The conclusions reached in this paper are not affected by uncertainties in the absolute energy measurements of this magnitude.

We have found that the electrostatic analyzer will not pass ions with energies less than about 1.5 eV. It has been determined experimentally that this cutoff is not due to stray fields in the chamber. We have also verified that it is not due to alkali dosing or patch fields on the surface of the analyzer spheres. The cutoff limits the minimum measurable energy, but does not influence our conclusions.

The sample is cleaned by sputtering with 1000 eV Ar^+ at $\approx 10\ \mu\mathrm{A/cm}^2$ followed by annealing to 600 °C for 2 min. The surface order and cleanliness are monitored using low-energy electron diffraction (LEED) and Auger electron spectroscopy. The sample is clean within Auger detection limits and well ordered according to LEED. The pressure in the chamber during an experiment is typically in the high 10^{-11} Torr range.

All the data presented in this work are taken at sample temperatures T_s between 121 and 141 K. The sample is cooled using a liquid-nitrogen reservoir attached to the sample holder with a copper braid. The sample temperature is monitored with a Chromel-Alumel thermocouple. Sample cooling is necessary in order to clearly resolve the energy-loss peaks in the energy spectra. The peak broadening, which is due to thermal vibrations of the surface atoms, has a larger fractional effect on the spectra for low incident energies (E_0). In fact, the peaks cannot be resolved at room temperature for $E_0 \leqslant 15$ eV, whereas they are easily resolved at $T_s = 140$ K. We have verified experimentally that, while the widths of the peaks are very sensitive to the sample temperature, the mean peak energies do not change. We discuss the temperature dependence of this peak broadening elsewhere.[8,9]

In order to ensure the accuracy of the measured energies and angles of the scattered ions a multistage alignment procedure is used.[10] The rotation axes of the sample and detector and the central axis of the beam line are aligned optically to within 0.25 mm using a He-Ne laser in conjunction with alignment apertures. The sample azimuth and tilt and the incident scattering angle (θ_i) are all aligned to within 0.5°

using a combination of LEED and keV ion scattering. Before each data set the alignment of the beam, sample, and detector is further refined using hyperthermal energy ion scattering.

For a given incident beam energy many sequential scattering spectra were taken without cleaning the sample. The effects of beam drift, sample dosing, and sample damage during such a data set were monitored by periodically taking reference spectra at a fixed scattering geometry and checking the beam current at the sample position using a Faraday cup. The mean peak energies in the reference spectra were unchanged during a data set, but the beam dosing reduced the scattering intensity (by up to 60% for some data sets) and slightly broadened the peaks. The intensity drop can be attributed to an increase in the neutralization probability of the scattered Na^+ caused by the reduction of the surface work function by trapped sodium.[11]

III. SIMULATIONS

At hyperthermal energies the incident ion interacts simultaneously with several surface atoms, resulting in complex scattering trajectories. Computer simulations are therefore necessary to interpret the results. Since the de Broglie wavelength of a 10-eV Na atom is 0.019 Å, even at the lowest energies in this study a classical description of the trajectory is appropriate. The trajectory calculations are performed with the computer code SAFARI, which has been described in detail elsewhere.[12] In SAFARI the trajectories are determined by integrating Hamilton's equations of motion. The ion interacts with the surface atoms through an interaction potential that is discussed in detail in Sec. IV.

In our simulations the energy loss of the scattering ion is due solely to momentum transfer to the recoiling surface atoms. We have not included losses to electronic excitations.[13–18] In order to test whether this is justified we have run some simulations where an additional frictional force on the ion was included to account for electronically inelastic losses.[10,13] This force, or stopping power, has been calculated using effective-medium theory[16,19] for an atom moving slowly ($v^{\text{ion}} \ll v^f$, where v^f is the Fermi velocity) through a homogeneous electron gas. According to the simulations, for typical trajectories at $\theta_i = \theta_f = 45°$ that do not penetrate the first layer, the additional energy transfer due to these electronically inelastic losses is $\leqslant 0.03$ eV for $E_0 = 10$ eV and $\leqslant 0.1$ eV for $E_0 = 100$ eV. These are much smaller than the energy loss due to momentum transfer to the recoiling surface atoms at $\theta_i = \theta_f = 45°$, which is $\geqslant 5.3$ eV for $E_0 = 10$ eV and $\geqslant 36$ eV for $E_0 = 100$ eV (see Fig. 4). Other more sophisticated models typically predict that the energy loss to electron-hole pair formation is less than a few tenths of an eV for ions interacting with metals at the velocities used in this study.[14,15,17,18] We therefore feel that we are justified in omitting losses to electronically inelastic processes from the present simulations.

The surface dynamics in the simulations are modeled by treating the surface atoms as though they are connected to their nearest neighbors by harmonic springs. The spring constant was determined by fitting to bulk phonon dispersion curves. The inclusion of these interatomic surface forces increases the effective mass of the surface atoms. This effect, however, is quite small: At $E_0 = 20.3$ eV the energy loss is decreased by only 0.02 eV when the nearest-neighbor forces are included.

Thermal motions of the surface atoms can also be included in the simulations. In this work, simulations were performed for both ''vibration-free'' surfaces, where the surface atoms are not initially vibrating about their equilibrium positions (i.e., no zero point or thermal motion) and for ''finite-T_s'' surfaces, where thermal displacements and momenta of the surface atoms are included. We have verified that when thermal motions are included in the simulations the peaks in the energy spectra are broadened, but the mean peak energies do not change significantly. Therefore we have used vibration-free surfaces in those simulations in which only the mean peak energy is of interest, since these simulations take considerably less computer time than the finite-T_s simulations. The experimentally observed peaks tend to be broader than those predicted by the finite-T_s simulations. All the simulations presented in this paper used vibration-free surfaces unless otherwise noted.

IV. INTERACTION POTENTIAL

The ion-surface interaction potential that describes hyperthermal energy alkali ion scattering from metal surfaces has been the focus of several recent studies. In order to provide some perspective on our work on this potential, we begin this section by briefly reviewing the results of some of these other studies. Since the energy and angular distributions of the scattered ions are very sensitive to the interaction potential, models for the potential can be tested by comparing measured scattering distributions to simulations in which the interaction potential is varied. Typically in these efforts the ion-surface interaction potential is constructed as a sum of repulsive pair potentials with, in some cases, an additional attractive term included to account for the image interaction.

Most of the work to date has concentrated on the repulsive part of the interaction potential. In several studies, for $E_0 = 12-100$ eV alkali scattering from W(110),[20–23] Kleyn and co-workers modeled the interaction potential as a sum of repulsive Born-Mayer pair potentials with an additional imagelike attractive term. They concluded that the scattering was sensitive to the form of the repulsive pair potentials, that the sum-of-pair potentials approximation broke down for trajectories that probed the hollow site, and that the attractive well in the interaction potential was not important even at incident energies below $E_0 = 35$ eV. The best-fit potential in this work contained five adjustable parameters and reproduced the data well for 25 eV$\leqslant E_0 \leqslant$45 eV, but there were discrepancies outside this energy range. In a later study they compared their data to simulations using a sum of Hartree-Fock-Slater (HFS) pair potentials with no free parameters and again found that the sum of pair potentials approximation failed to reproduce the scattering from trajectories that probed the hollow site. They concluded that this was due to insufficient repulsion in the hollow site by comparing the sum of pairs to a more accurate cluster calculation.[24] Subsequently they studied Na and K scattering at normal incidence from Ag(111) at incident energies ranging from 10 to 100 eV and found that they could reproduce many features of the measured scattering distributions using an interaction potential with no fitting parameters.[25] They used a purely repulsive potential constructed from a sum of HFS pair potentials and found that, in this case, the sum of pair potentials approximation did not break down. They attributed the discrepancies between the data and simulations at the lowest incident energies ($E_0 \leqslant 35$ eV) to the influence of the attractive image interaction, which was not included in the simulations.

Over the past few years we have made detailed studies of the potential for 50–400 eV alkali ion scattering from Cu(001) (Ref. 26) and Cu(110) (Refs. 13, 27, and 28) using the classical trajectory simulation code SAFARI.[12] In these studies the repulsive part of the potential was modeled as a sum of Hartree-Fock (HF) pair potentials.[13] The simulations using the HF pairs were in excellent agreement with the data, whereas simulations using the universal Ziegler-Biersack-Littmark pair potential[29] were not, demonstrating the sensitivity of the scattering to the repulsive part of the potential. In addition, we concluded, in contrast to the previous studies described above, that including an additional attractive term to account for the image interaction significantly improved the agreement between the simulated and measured scattering distributions at these incident energies. However, the scattering was not sensitive enough to the attractive interaction to allow a detailed characterization of the attractive well because the incident energy E_0 was large compared to the well depth.

In this paper we make a detailed comparison of measured and simulated scattered ion distributions for 10–100 eV Na^+ scattering from Cu(001), with an emphasis toward understanding how the attractive interaction influences the scattering and trapping dynamics. Hulpke previously recognized the importance of the attractive well in his study of the energy loss of 2–20 eV Li^+ scattering from W(110),[30] in which he used a square well to account for the image interaction. The importance of the attractive well has also been noted in other studies for hyperthermal alkali[31] and reactive ion[32,33] scattering from metal surfaces.

Below we discuss both the attractive and repulsive parts of the total interaction potential used in the current studies. A detailed discussion of the calculation of the repulsive term can be found in the Appendix. As we demonstrate in this paper, simulated scattering distributions using this total potential are in excellent agreement with the data for 10 eV$\leqslant E_0 \leqslant 100$ eV Na^+ scattering from Cu(001). The only significant difference between this potential and that determined in our previous work at 50 eV$\leqslant E_0 \leqslant 400$ eV is the parametrization of the attractive term (see below). Therefore, since the scattering behavior is not sensitive to the details of the attractive well for $E_0 > 100$ eV, the potential described in this work should also be valid up to $E_0 = 400$ eV.

The ion interacts with the surface atoms through an interaction potential that consists of two parts. The first part is constructed from a sum of repulsive pair potentials and the second is a long-range attractive term to account for the interaction of the ion with its image charge in the metal. The details of both parts of the interaction potential are very important in determining the scattered trajectories and energy transfer.

Here we note some of the important features of the potential, concentrating the discussion on the attractive term. The repulsive $(\text{Na-Cu})^+$ pair potential, which is calculated using Hartree-Fock is summed over the six or more surface atoms nearest the scattering ion at each point in its trajectory (see the Appendix for details). An attractive term is added to the sum of pair potentials to form the total potential used in the simulations. The attractive term, which has also been used in previous studies,[13,20–22,28,31,34] is of the form

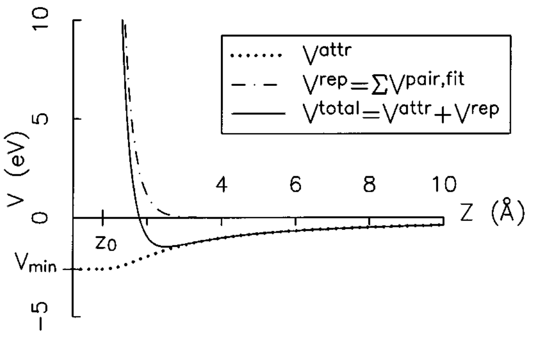

FIG. 2. Repulsive potential, constructed from a sum of Hartree-Fock $(\text{Na-Cu})^+$ pair potentials; the attractive term to account for the image potential; and the total potential ($V_{\min}=2.6$ eV and $z_0=0.8$ Å) are plotted as a function of distance z from the surface, directly above a top layer atom. Simulations using this parametrization ($V_{\min}$ and z_0) of the attractive term are in excellent agreement with all the data.

$$V_{\text{attr}}(z) = \begin{cases} -e^2/\sqrt{16(z-z_0)^2 + e^4/V_{\min}^2} & \text{if } z > z_0 \\ -V_{\min} & \text{if } z \leqslant z_0, \end{cases} \tag{1}$$

where z is the perpendicular distance from the top plane of atoms and z_0 is the maximum value of z for which $V_{\text{attr}} = -V_{\min}$. This form reduces to the $1/4z$ classical image potential far from the surface and saturates near the surface to the value $-V_{\min}$. The values of $V_{\min}$ and z_0 are the only adjustable parameters in the total potential. Note that the parameter $V_{\min}$ is not the well depth D in the total potential (see Fig. 2). In general, $D \leqslant V_{\min}$, with D approaching $V_{\min}$ as z_0 is increased.

In our previous work, at 100 eV and higher energies, we found that the potential including this form for V_{attr} gave very good agreement with measured energy spectra when $V_{\min}$ was chosen to be 3 eV and z_0 was set equal to 0 Å.[13,27,28] In this paper we have exploited the enhanced sensitivity of the scattering to the attractive potential at $E_0 \leqslant 100$ eV to refine our parametrization of the attractive well. Although there is a range of parametrizations of our model potential that reproduce our experiments, the agreement is particularly good for $V_{\min}=2.6$ eV and $z_0=0.8$ Å (see Sec. VI). We refer to the potential constructed with this parametrization as ''the total potential.''

The parameter z_0 plays a role similar to that of an image plane. Assuming a jellium surface with the electron density of copper, the position of the image plane is located 1.7 Å from the surface.[35] However, there have been recent theoretical results that indicate the image plane may be closer to the surface than the jellium result.[36,37] When the jellium value of the image plane position is used for z_0 in our model potential, the agreement between simulation and data is acceptable, but not as good as the agreement for the total potential.

The total potential is shown in Fig. 2 as a function of distance z from the surface above a top-layer atom. The re-

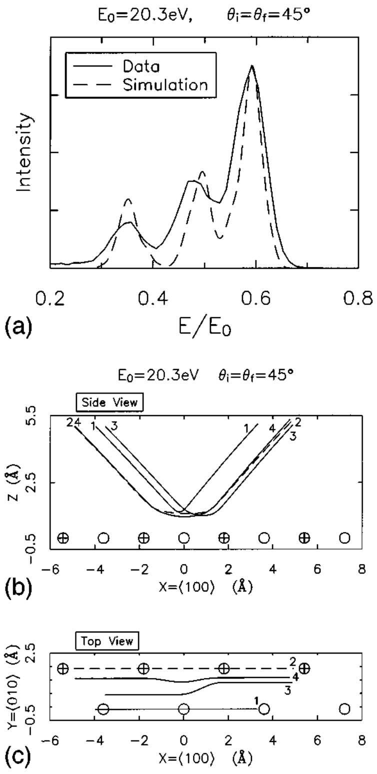

FIG. 3. (a) Measured and simulated energy spectra are compared for $E_0 = 20.3$ eV and the 90° specular scattering geometry. The total potential shown in Fig. 2 is used in the simulation and thermal vibrations are included. The data have been corrected for the detector transmission function (see the text). (b) Side view of the types of trajectories that contribute to the simulated energy spectrum. Trajectory 1 (quasisingle, QS) contributes to the lowest-energy peak, trajectory 3 (double zigzag, DZZ) to the middle energy peak, and trajectories 2 (quasidouble, QD) and 4 (triple zigzag, TZZ) to the highest-energy peak. Top layer atoms are indicated by circles and circles with crosses in adjacent ⟨100⟩ chains. (c) Top view of these trajectories.

pulsive and the attractive terms are plotted separately. This total potential features an attractive well with a depth of 1.5 eV located 2.5 Å from the surface for the on-top site (Fig. 2) and an attractive well with a depth of 1.7 eV located at 2.05 Å for the hollow site [above the second-layer atom; see Fig. 1(a)]. Although the scattering distributions are very sensitive to the presence of the attractive term, our data are consistent with a range of parametrizations of the potential (i.e., a range of $V_{\min}$ and z_0) and therefore the scattering is somewhat insensitive to the details of the shape and depth of the attractive well. For example, parametrizations with well depths at the on-top site ranging from 1.3 to 2.6 eV are in agreement with the data (see Sec. VII C for further discussion).

V. ENERGY SPECTRA AND TRAJECTORY ANALYSIS

In hyperthermal energy ion-surface scattering there are generally several peaks that correspond to different trajectory types in an energy spectrum at a fixed scattering geometry. The determination of the trajectories from comparisons of SAFARI simulations and measured energy spectra is illustrated in Fig. 3. In Fig. 3(a) a measured energy spectrum is compared to a simulated one for Na^+ at $E_0 = 20.3$ eV and a 90° specular scattering geometry, i.e., $\theta_i = \theta_f = 45°$ [see Fig. 1(b)]. The surface temperature was $T_s = 123$ K. The scattered intensity is plotted as a function of the reduced energy E/E_0 of the scattered particles, where E_0 is the incident beam energy and E is the scattered ion energy. The intensity of the measured energy spectrum is multiplied by $1/E$ to correct for the transmission function of the detector and facilitate comparison to the simulation. The simulated energy spectrum was generated from a $T_s = 130$ K SAFARI simulation using the total potential. The detector in the simulation was circular with a 3° half angular acceptance and an energy resolution of 0.4 eV. The angular acceptance and the energy resolution of the simulated detector are larger than those of the experimental detector. This reduces the computer time and increases the peak widths in the simulations. The mean energies of the peaks and the relative peak intensities are not significantly influenced by the enlarged detector used in the simulation.

The agreement between the data and simulation is excellent. In particular, the mean energies of the peaks are reproduced well by the simulation. According to the simulation, the three peaks in the energy spectrum correspond to four different types of scattering trajectories. Typical examples of these trajectories, taken from a vibration free simulation, are shown from both side and top views in Figs. 3(b) and 3(c), respectively. There are two chainlike trajectories involving atoms only along top-layer chains in the ⟨100⟩ azimuth: quasisingle scattering, where momentum transfer is primarily to one surface atom, and quasidouble scattering, where momentum transfer is to two adjacent atoms along the chain. These are trajectories 1 and 2, respectively, in Figs. 3(b) and 3(c). The other two trajectory types are zigzag collisions involving momentum transfer to atoms in adjacent ⟨100⟩ chains. A double zigzag trajectory and triple zigzag trajectory are shown as trajectories 3 and 4, respectively. An energy analysis of the trajectories[26] indicates that the lowest peak in the corresponding energy spectrum is composed of chainlike quasisingle (QS) scattering ($E/E_0 = 0.35$, trajectory 1), the middle peak of double zigzag (DZZ) scattering ($E/E_0 = 0.49$, trajectory 3), and the highest-energy peak of chainlike quasidouble (QD) scattering ($E/E_0 = 0.59$, trajectory 2) and triple zigzag (TZZ) scattering ($E/E_0 = 0.59$, trajectory 4). Recall that the only energy-loss mechanism included in the simulations is momentum transfer to the recoiling surface atoms.

When the same scattering geometry is used, this same three peak structure is observed for $10\ \mathrm{eV} \leqslant E_0 \leqslant 100$ eV. This is demonstrated in Fig. 4, where energy spectra corresponding to different E_0 are offset vertically and the maximum peak heights are normalized. Simulations indicate that the trajectory assignments for the peaks at $E_0 = 20.3$ eV hold throughout this energy range with only two exceptions. At $E_0 = 100.6$ eV the triple zigzag peak appears as a high-energy shoulder on the double zigzag peak and the quasisingle peak at $E_0 = 9.7$ eV appears as a low-energy shoulder on the double zigzag peak. The relative peak heights, the value of E/E_0 for each peak, and the fractional widths of the peaks all change as a function of E_0. Although these trends are discussed in detail in Sec. VII, we describe here how the attractive term in the potential influences the trajectories and

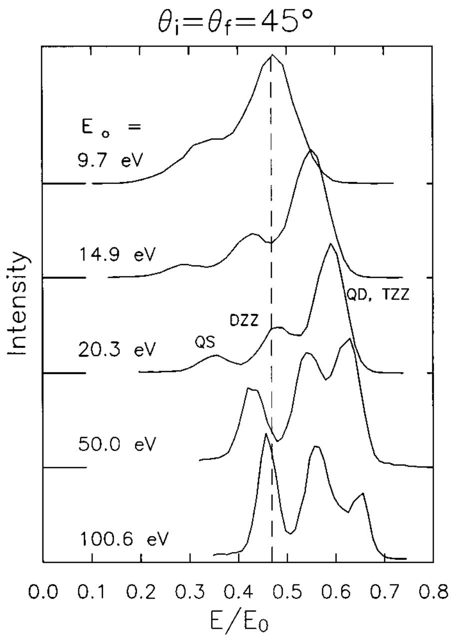

FIG. 4. Measured energy spectra are compared for the 90° specular scattering geometry. Spectra corresponding to different E_0 ranging from 9.7 to 100.6 eV are offset vertically. The spectra have been corrected for the detector transmission function by multiplying the intensity by $1/E$. The dashed line indicates the kinematic factor ($E/E_0=0.47$) for a pure single collision. There is an additional peak at $E/E_0<0.1$ in the $E_0=100.6$ eV spectrum that is not shown here (see Fig. 13).

the fractional energy loss, as this is a central point in this paper.

The increase in the fractional energy loss with decreasing E_0 can be understood by considering energy transfer in a pure binary collision and comparing it with the energy transfer in a quasisingle collision between Na$^+$ and a Cu surface. In a pure binary collision between a projectile of mass m_p and a stationary target atom of mass m_t, the ratio of the projectile's scattered energy to its incident energy can be expressed as $E/E_0=k(\theta_{\mathrm{TSA}},\mu)$, where $\mu=m_p/m_t$ and $\theta_{\mathrm{TSA}}=180°-\theta_i-\theta_f$ is the total scattering angle[38] (see Fig. 1). The kinematic factor $k(\theta_{\mathrm{TSA}},\mu)$ is derived from energy and momentum conservation and is given by

$$E/E_0=k(\theta_{\mathrm{TSA}},\mu)$$

$$=\left(\frac{\mu}{1+\mu}\right)^2\left[\cos\theta_{\mathrm{TSA}}+\sqrt{\frac{1}{\mu^2}-\sin^2\theta_{\mathrm{TSA}}}\right]^2. \qquad (2)$$

This result is valid for elastic collisions in which the projectile and target interact only through a central force that vanishes at large separations. Note that Eq. (2) implies that in this case the fractional energy transfer

$$\Delta E/E_0=1-k(\theta_{\mathrm{TSA}},\mu) \qquad (3)$$

to the target atom is independent of both E_0 and the details of the potential.

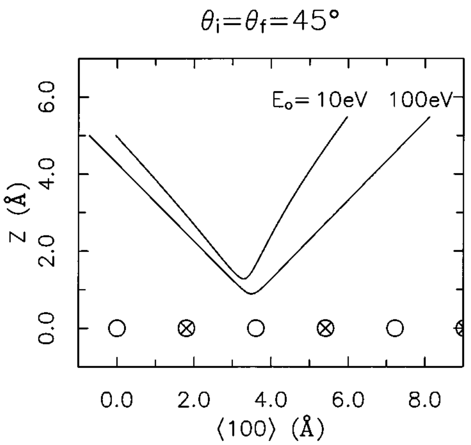

FIG. 5. Comparison of the simulated quasisingle trajectories for the specular scattering geometry at $E_0=10$ and 100 eV. The near surface total scattering angle is larger at $E_0=10$ eV due to trajectory bending by the image force.

In Fig. 4 the predicted value of $E/E_0=0.47$ from Eq. (2) for Na$^+$ scattering from Cu through an angle $\theta_{\mathrm{TSA}}=90°$ is indicated by the dashed line. The measured fractional final energies of the QS peaks, however, are not independent of E_0, but vary from $E/E_0\approx 0.2$ for $E_0=9.7$ eV to $E/E_0=0.45$ for $E_0=100.6$ eV. As is discussed in the paragraphs that follow, a qualitative understanding of this trend can be obtained by considering how to modify Eqs. (2) and (3) to account for the image interaction between the ion and the conduction electrons in the metal. This image interaction produces an attractive force that depends on the distance z from the surface and therefore violates one of the requirements necessary for the validity of Eqs. (2) and (3), namely, that the potential depend only on the projectile-target atom relative coordinates. This additional force modifies the trajectories, introducing an E_0 dependence to the fractional energy transfer.

The image force accelerates the ion towards the surface. As a result, in the near surface region the precollision incident energy is increased and trajectory bending results in a larger total scattering angle during the collision. These trajectory modifications result in an increased fractional energy transfer to the surface that becomes more pronounced as the incident energy is reduced. The trajectory bending is illustrated in Fig. 5, which shows simulated QS trajectories in the near surface region for $E_0=10$ and 100 eV under the same scattering conditions as in Fig. 4. Asymptotically $\theta_{\mathrm{TSA}}=90°$ for both trajectories, but in the near-surface region the scattering angle is increased due to trajectory bending by the attractive force, particularly at $E_0=10$ eV.

Here we give a simple model, based on a modification of the pure binary collision picture, that accounts for the influence of the attractive potential on the trajectory. A more complete discussion of the energy dependence of the fractional energy transfer, including the influence of simultaneous interaction with multiple surface atoms, can be found in Sec. VII. In the simple model, Eq. (3) is modified to account for the case when the ion is preaccelerated towards the surface atom, subsequently scatters in a pure binary collision, and then decelerates after the collision. For simplicity, we assume that the attractive and repulsive forces act sequentially in this analysis. The validity of this assumption is discussed in Sec. VII C. If the asymptotic values of the incident energy, final energy, and total scattering angle are E_0, E, and θ_{TSA}, then in the near surface region they are given by E_0+D, $E+D$, and $\theta_{\rm TSA}+\Delta\theta$, respectively, where D is the increase in the incident energy due to the attractive force and $\Delta\theta$ is the increase in the total scattering angle. The energy transfer in this case is

$$\Delta E/E_0=[1+D/E_0][1-k(\theta_{\rm TSA}+\Delta\theta,\mu)]. \qquad (4)$$

Since $\Delta\theta$ is an increasing function of D/E_0 (see Fig. 5) and $[1-k(\theta_{\rm TSA}+\Delta\theta,\mu)]$ is an increasing function of $\Delta\theta$, the fractional energy transfer according to Eq. (4) increases monotonically with D/E_0. This is consistent with the energy shifts in the peaks observed in Fig. 4. In fact, if we measure $\Delta\theta$ from the simulated trajectories in Fig. 5 and use the depth of the attractive well in Fig. 2 for D ($D=1.5$ eV), then Eq. (4) yields $E/E_0=0.24$ for $E_0=9.7$ eV and $E/E_0=0.45$ for $E_0=100.6$ eV, which are in good agreement with the experimental results in Fig. 4. We note here that similar extensions to the pure binary collision model to account for the attractive well have been discussed previously by Hulpke for hyperthermal scattering.[30] There are additional, more subtle ways in which the attractive well affects the energy loss. These are discussed in Sec. VII C.

The three peak structure of the energy spectra in this scattering geometry for $E\geqslant E_{\rm QS}$, where $E_{\rm QS}$ is the QS peak energy, is actually observed for 100 eV$<E_0<$1000 eV as well. According to the simulations, however, additional types of trajectories begin to contribute to the spectra for $E_0>200$ eV. It is interesting to note that the relatively simple evolution of the energy spectra as a function of incident energy observed for this scattering geometry is fortuitous. In studies of scattering along the ⟨110⟩ azimuth, the energy spectra exhibit more complicated behavior as a function of incident energy for $E\geqslant E_{\rm QS}$. Simulated and measured energy spectra show that for scattering Na$^+$ from Cu(001)⟨110⟩ in the same scattering geometry and the same incident energy range as in Figs. 3 and 4, new types of trajectories start to contribute to the spectra for $E\geqslant E_{\rm QS}$ as the incident energy is increased from 10 to 100 eV.[26] This makes it more difficult to interpret the influence of the attractive well on energy losses in this case.

In general, for $E\leqslant E_{\rm QS}$ and/or final angles other than $\theta_f=45°$ there are additional types of trajectories that make significant contributions to the energy spectra. We have studied such peaks at $E_0\geqslant 50$ eV and θ_f close to the surface normal. These peaks, which typically appear at energies lower than the quasisingle peak, are of interest here primarily because they provide additional evidence for the accuracy of the simulations and the interaction potential. In Fig. 6(a) a measured energy spectrum is compared with a simulated one for Na$^+$ scattering from Cu(001)⟨100⟩ at an incident angle of $\theta_i=45°$ and a final angle of $\theta_f=10°$. The peak positions in the simulations are in excellent agreement with the data, but the relative intensities are not. This discrepancy is due to charge transfer effects that are discussed at the end of this section.

In contrast to the spectra in Fig. 4, there are five peaks in both the measured and simulated energy spectra in Fig. 6(a). Trajectory analysis indicates that the three highest-energy peaks consist of quasisingle trajectories ($E/E_0=0.27$), double zigzags ($E/E_0=0.34$), and quasidouble and triple zigzag trajectories ($E/E_0=0.39$). The two low-energy peaks are due to additional trajectory types that do not contribute to the scattering at $\theta_f=45°$. Examples of these new types of trajectories are shown in Figs. 6(b) and 6(c), which show side views and top views of the trajectories, respectively. The lowest-energy peak in Fig. 6(a) consists primarily of trajectories like trajectory 5 in Figs. 6(b) and 6(c) and the second lowest-energy peak consists primarily of trajectories similar to trajectory 6. Trajectory 5 is a chainlike scattering event involving large total scattering angle collisions with a first-layer atom, a second-layer atom, and a first-layer atom again. We refer to this trajectory type as a kinked chain (KC) trajectory. The kinked chain trajectory loses a large fraction

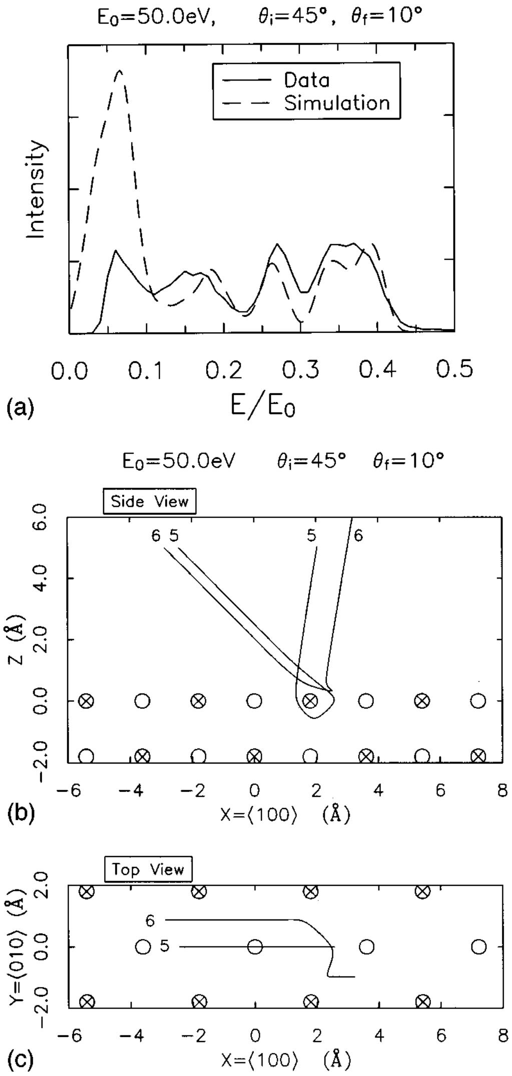

FIG. 6. (a) Measured and simulated energy spectra are compared for $E_0=50.0$ eV and $\theta_f=10°$. The measured spectrum has been corrected for the detector transmission function by multiplying the intensity by $1/E$ and thermal vibrations have been included in the simulation ($T_s=130$ K). (b) Side view of the types of trajectories that contribute to the two lowest-energy peaks in the spectra. Trajectory 5 (kinked chain, KC) contributes to the lowest-energy peak and trajectory 6 (kinked zigzag, KZZ) contributes to the peak at $E/E_0=0.18$. The three high-energy peaks have the same trajectory assignments as the peaks in Fig. 3. Top- and second-layer atoms are indicated by circles. Atoms located either 1.805 Å in or out of the plane of the figure are indicated by circles with crosses. (c) Top view of these trajectories. Only the top layer atoms are shown.

of its energy ($E/E_0=0.065$) due to the multiple large-scattering-angle collisions it undergoes. Trajectory 6 corresponds to collisions with three top-layer atoms belonging to three adjacent ⟨100⟩ chains of atoms. We refer to trajectories of this type as kinked zigzag (KZZ) trajectories. It is not surprising that the kinked zigzag trajectories lose a large fraction ($E/E_0=0.18$) of their incident energy since they, like the kinked chain trajectories, undergo multiple large-angle collisions. There are other types of trajectories, besides the two discussed here, that also contribute to the scattering at energies below the quasisingle peak, but they have much smaller scattering cross sections and therefore make smaller contributions to the energy spectra.

The ratio of the intensity of lowest energy peak ($E/E_0=0.065$) to the peak at $E/E_0=0.27$ is about three times larger in the simulations than in the data. By using a neutral alkali detector[39] as part of a time-of-flight energy analyzer, we have verified that about half of the discrepancy is due to enhanced neutralization of the trajectories that contribute to the lowest-energy peak. This peak consists primarily of the KC trajectories, which penetrate the first layer of the surface [see Figs. 6(b) and 6(c)]. Since the electrostatic analyzer used to measure the spectrum in Fig. 6(a) can only detect ions, the enhanced neutralization results in a relatively smaller measured intensity in the lowest-energy peak. The simulations do not include the possibility of charge transfer between the ion and the surface. As a result, if there is trajectory-dependent neutralization the relative peak heights in the simulations and data will not agree. This usually is not a problem since it has been observed that when the ions do not penetrate the first layer the charge transfer probability varies by less than 10% across a given spectrum in this energy range for alkalis scattering from Cu(001)⟨100⟩.[40]

VI. COMPARISON OF DATA AND SIMULATIONS: ENERGY-θ PLOTS

So far we have discussed the energy spectra at a fixed scattering geometry. A more complete picture of the scattering for a fixed E_0 and θ_i, including both the scattered energy and angular distributions, can be obtained by generating an energy-θ plot.[28,34,38,41,42] In the following subsection we describe the construction of such plots from measured energy spectra for Na^+ scattering from Cu(001)⟨100⟩ at $\theta_i=45°$ and $9.7\ \mathrm{eV}\leqslant E_0\leqslant 100.6$ eV and compare them with simulations. The simulations using the total interaction potential are in excellent agreement with data for the full range of E_0, demonstrating the accuracy of the potential and the simulations. The importance of the image potential in determining both the energy and angular distributions is demonstrated by noting that at low E_0 there is poor agreement between the data and simulations that use only the repulsive part of the potential.

A. Construction of energy-θ plots

The procedure for constructing an energy-θ plot from the data is illustrated in Figs. 7 and 8(a). Figure 7 shows a series of energy spectra measured at different final angles for $E_0=20.3$ eV. The spectra corresponding to different final angles are offset vertically in the plot: $\theta_f=0°$ corresponds to scattering along the surface normal and $\theta_f=90°$ corresponds to scattering parallel to the surface.

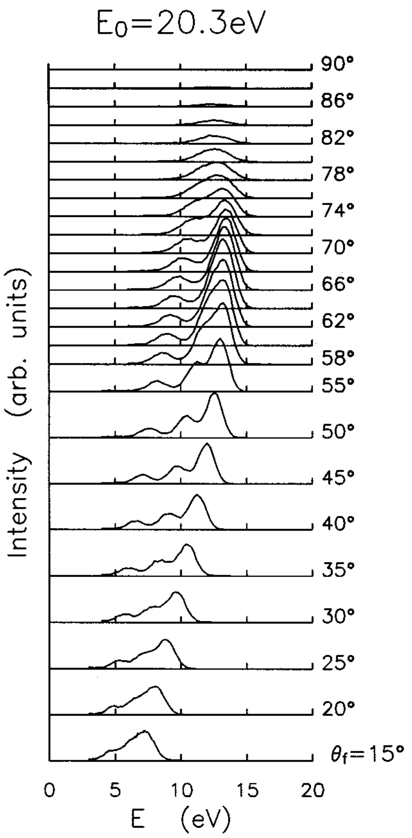

FIG. 7. Energy spectra measured as a function of θ_f for $E_0=20.3$ eV and $\theta_i=45°$. The spectra corresponding to different θ_f are offset vertically. The spectra have been corrected for the detector transmission function by multiplying the intensity by $1/E$.

The energy-θ plot corresponding to the data in Fig. 7 is shown in Fig. 8(a) (open circles), where the reduced energies, i.e., E/E_0, of the peaks in the energy spectra are plotted as a function of θ_f. The energies of the peaks are determined by fitting a sum of either two or three Gaussians to the energy spectra in Fig. 7, depending on the number of peaks in the spectrum. The mean energies, amplitudes, and standard deviations of the Gaussians are treated as free parameters in the fits. Using this technique makes it possible to extract the energies of overlapping peaks, such as the two high-energy peaks at $\theta_f=58°$ in Fig. 7.

The measured energy-θ plot[28] in Fig. 8(a) has three branches that form portions of two ''loops.'' In the trajectory analysis of the energy spectrum at $\theta_f=45°$ [see Figs. 3(a)–3(c)] we found that the low-energy peak was due to QS trajectories, the intermediate peak to DZZ trajectories, and the high-energy peak to both QD and TZZ trajectories. Further analysis indicates that the different branches of the measured energy-θ plot in Fig. 8(a) can be attributed to these same four different trajectory types. They are defined as follows: for a scattering angle $\theta_f=45°$ the QS peak ($E/E_0=0.35$) lies on the *lower branch*, the DZZ peak ($E/E_0=0.48$) lies on the *middle branch*, and the QD-TZZ peak ($E/E_0=0.59$) lies on the *upper branch*. The upper and lower branches in the energy-θ plot lie on an energy-θ loop corresponding to chainlike scattering; the lower branch re-

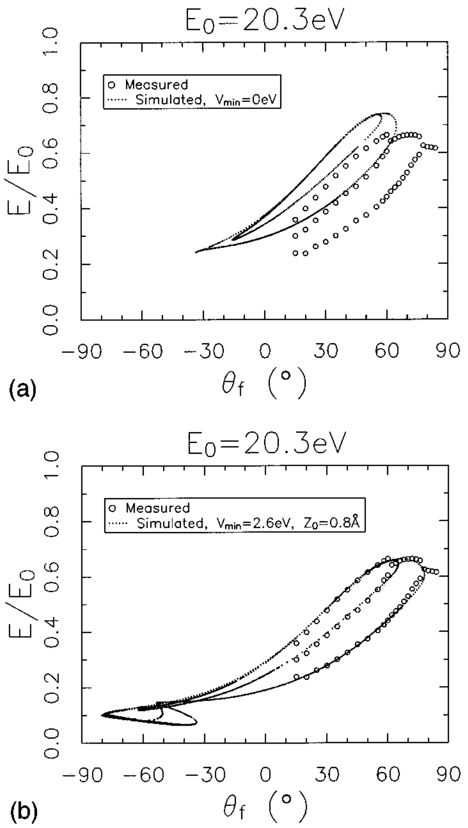

FIG. 8. (a) Measured energy-θ plot for $E_0 = 20.3$ eV constructed from the data in Fig. 7, compared to a simulation in which only the repulsive part of the scattering potential (see Fig. 2) is used. (b) Same as (a), except that the total potential, which includes the attractive well, is used in the simulation.

sults from different impact parameters along the ⟨100⟩ chain that lead to QS scattering into different final angles. Likewise, the QD chain trajectories contribute to the upper branch. The middle and upper branches lie on the loop for zigzag scattering, with the DZZ trajectory in the middle branch and the TZZ in the upper branch. Thus the upper branch forms parts of both the chain and zigzag loops. The chain and zigzag loops are prominent features in the energy-θ plots for 10 eV$\leqslant E_0 \leqslant$100 eV.

B. Rainbow scattering

There are two pairs of energies and angles at which branches of the measured energy-θ plot merge in Fig. 8(a). These are both ''forward'' rainbows. The rainbows are due to local extrema in the differential scattering cross section and result in peaks in the angle-resolved scattering distributions.[38,41,43,44] Rainbow scattering has been observed for incident energies ranging from thermal ($E_0 < 1$ eV) to several keV (see Ref. 44 and references therein). The rainbow at $\theta_f = 62° \pm 2°$ and $E/E_0 = 0.66$ is associated with the zigzag loop and is called the zigzag rainbow and the rainbow at $\theta_f = 78° \pm 2°$ and $E/E_0 = 0.63$ is associated with the chain loop and is called the chain rainbow.

For a perfectly ordered surface with no thermal displacements of the surface atoms, the rainbows represent divergences in the differential scattering cross section. In addition, one does not expect any zigzag scattering (DZZ and TZZ) at angles larger (i.e., further from the surface normal) than the zigzag rainbow angle, nor any chain scattering (QS and QD) at angles larger than the chain rainbow angle. However, note that there is some scattering apparent for $\theta_f > 78°$ (see Fig. 7). These low-intensity scattering features are due to the presence of both thermal vibrations of the surface atoms and possibly to surface disorder.[45,46] These factors, along with the ±0.5° angular acceptance of the detector, result in broadened peaks in the angular distributions at the rainbow angles. In Fig. 7 the intensity maximum as a function of θ_f associated with the zigzag rainbow ($\theta_f = 62° \pm 2°$) is fairly clear, whereas the maximum associated with the chain rainbow ($\theta_f = 78° \pm 2°$) is not. These maxima might be more clearly separated if the angular resolution of the detector was improved.

C. Data vs simulation, $E_0 = 20.3$ eV

In Figs. 8(a) and 8(b) the experimental (open circles) energy-θ plot corresponding to the spectra in Fig. 7 for $E_0 = 20.3$ eV is compared to two simulated (small dots) energy-θ plots using different ion-surface interaction potentials. Thermal vibrations were not included in the simulations, since including them increases the computational time without affecting the energy losses or the rainbow angles of the scattered flux. The simulated energy-θ plots represent the final energies and angles of the trajectories that fall within ±0.25° of in-plane scattering, which is defined as the plane containing the axis of the incoming beam and the surface normal. The density of points in the simulated energy-θ plots is *not* related to the scattered intensity, but is an artifact of the adaptive grid technique of selecting the impact parameters.[12]

A simulation using only the purely repulsive sum of HF $(\mathrm{Na\text{-}Cu})^+$ pair potentials (see Fig. 2, dot-dashed line) is compared with the data in Fig. 8(a) and a simulation using the total potential (see Fig. 2, solid line), which includes the attractive term, is compared with the data in Fig. 8(b). It is clear that the simulation using the total potential is in much better agreement with the data, reproducing both the measured peak energies and the forward rainbow angles. From these simulations, it is evident that the attractive part of the interaction is very important in determining the final energies and angles of the scattered ions. Including the attractive term increases the energy loss to the surface, broadens the angular distribution of the scattered ions, and shifts the forward rainbow angles further from the surface normal (i.e., closer to grazing) due to the trajectory bending.

D. Data vs simulation, $E_0 = 9.7$ eV: Trapping

Figures 9(a) and 9(b) show measured and simulated energy-θ plots for $E_0 = 9.7$ eV. The lower branch, due to QS scattering, was not included in the data for $\theta_f < 45°$ because the cutoff in the detector transmission function at $E \approx 1.5$ eV makes determining the peak energy difficult. As was the case at $E_0 = 20.3$ eV, the upper and middle energy branches are due to QD/TZZ and DZZ scattering, respectively. These branches cannot be resolved at $\theta_f \leqslant 25°$ because of the enhanced thermal broadening of the peaks at low E_0 (see Fig. 4).

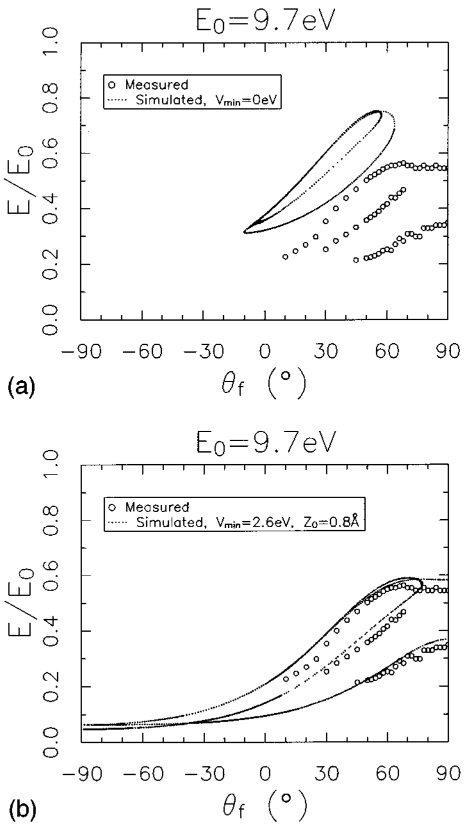

FIG. 9. (a) Measured energy-θ plot for $E_0 = 9.7$ eV compared to a simulation in which only the repulsive part of the scattering potential (see Fig. 2) is used. (b) Same as (a), except that the total potential is used in the simulation. The QS and QD branches extend to $\theta_f = 90°$ (parallel to the surface), indicating trapping of the trajectories that contribute to the forward chain rainbow located at $\theta_f = 63°$ in (a).

The simulation in Fig. 9(a) uses the same purely repulsive potential as in Fig. 8(a) and the simulation in Fig. 9(b) uses the total potential. As was the case for $E_0 = 20.3$ eV scattering, the simulation that includes the attractive term is in excellent agreement with the data, in contrast to that using the purely repulsive potential. Note that the chain rainbow is missing from both the data and the simulation in Fig. 9(b) and a gap in the chain loop (at $\theta_f = 90°$) is formed since the upper and lower branches (due to QD and QS scattering, respectively) extend to $\theta_f = 90°$, which corresponds to scattering parallel to the surface plane. In the simulation employing the purely repulsive potential a forward chain rainbow is found in the scattered flux at $\theta_f \approx 63°$ and $E/E_0 \approx 0.71$.

According to the simulations, the trajectories that contribute to the forward chain rainbow when the purely repulsive potential is used are *trapped* on the surface by the attractive well when the total potential is used. The gap at $\theta_f = 90°$ in Fig. 9(b) therefore indicates trapping. There is also a gap in the simulated energy-θ plot using the total potential at $\theta_f = -90°$ and $E/E_0 \approx 0.055$. This gap indicates the trapping of the trajectories that contribute to the backward chain rainbow [Fig. 9(a), $\theta_f = -10°$ and $E/E_0 \approx 0.31$] and backward zigzag rainbow [Fig. 9(a), $\theta_f \approx -5°$ and $E/E_0 \approx 0.34$] that appear in the simulation using the purely repulsive potential.

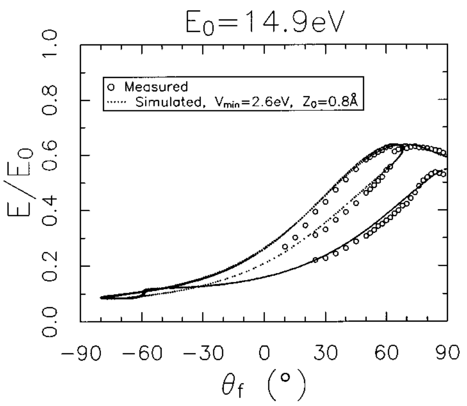

FIG. 10. Measured energy-θ plot for $E_0 = 14.9$ eV compared to a simulation using total potential (see Fig. 2). The gap in the plot at $\theta_f = 90°$ indicates trapping.

It is clear from Figs. 9(a) and 9(b) that the attractive term dramatically influences the scattering at $E_0 = 9.7$ eV. In the simulation employing the purely repulsive potential the scattered energies range from $0.31 < E/E_0 < 0.76$ and the range of final angles is constrained to $-10° < \theta_f < 64°$. In contrast, when the total potential including the attractive term is used, the trajectory bending causes the ions to scatter into all final angles ($-90° \leq \theta_f \leq 90°$), the fractional final energies are much lower ($0.04 < E/E_0 < 0.60$), and most of the rainbows are removed from the scattered flux due to trapping. The removal of rainbows due to both trapping and embedding has been discussed previously in the literature.[25]

Determining the ultimate fate of the trapped trajectories, i.e., whether the ion rescatters from the surface or sticks to it, is beyond the scope of these simulations. Accurate simulations of the trapping and embedding must account for the possibility of charge transfer and would require a more sophisticated model of the surface dynamics. The current simulations can, however, give detailed information on the trapping mechanisms and provide a qualitative measure of the trapping probability, as is discussed in more detail in Sec. VII D.

E. Data vs simulation, $E_0 = 14.9$ eV

We have observed a gap in the chain loop at $\theta_f = 90°$ in both measured and simulated energy-θ plots at other incident energies as well. This is demonstrated in Fig. 10, which shows a measured and simulated energy-θ plot for $E_0 = 14.9$ eV. The total potential is used in the simulation. Trapping has also been observed for $E_0 = 10.9$ eV. It is apparent from these gaps in the chain loop [for Na^+ scattering at $\theta_i = 45°$ on Cu(001)⟨100⟩] that as E_0 is reduced the onset of trapping of in-plane, forward-scattered Na^+ occurs at an incident energy 14.9 eV$< E_0 <$20.3 eV.

F. Data vs simulation, $E_0 = 30.4$ eV

In Fig. 11 a measured energy-θ plot is compared to a simulated energy-θ plot for $E_0 = 30.4$ eV. The simulation is calculated using the total potential. The measured and simulated energy-θ plots are in excellent agreement for the chain and zigzag loops, but the additional low-energy branches predicted by the simulation at $E/E_0 < 0.05$ and $\theta_f \geq 6°$ are not seen in the data. These branches cannot be observed in the experiments because their energies fall below the 1.5-eV

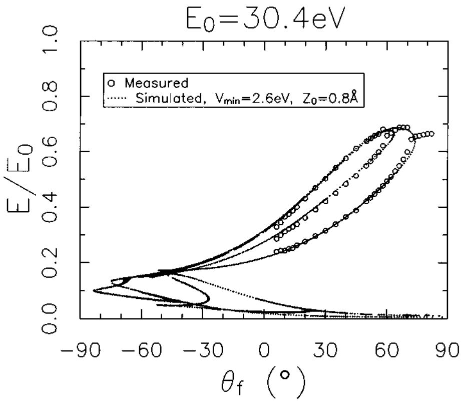

FIG. 11. Measured energy-θ plot for $E_0 = 30.4$ eV compared to a simulation using the total potential (see Fig. 2). The low-energy branches ($E/E_0 < 0.1$) in the simulation are below the detector cutoff energy in the experiments.

cutoff in the transmission function of the analyzer. Low-energy branches similar to these start to appear at this scattering geometry for 20.3 eV$< E_0 <$30.4 eV in simulations using the total potential.

G. Data vs simulation, $E_0 = 50.0$ eV

Figure 12 shows measured and simulated energy-θ plots for $E_0 = 50.0$ eV. The total potential was used in the simulation. As was the case at 20.3 eV, the agreement between calculation and experiment is improved considerably when the attractive term is included. According to the simulations, the energies and angles of the features at low E/E_0 (i.e., below the QS branch) are sensitive to both the attractive and repulsive terms in the interaction potential.

The structures of both the measured and simulated energy-θ plots at $E_0 = 50.0$ eV are more complex than at lower E_0, with numerous branches appearing in the data at low energy ($E/E_0 \leq 0.2$) in addition to the chain and zigzag loops ($E/E_0 \geq 0.25$). Although the simulation predicts several of these additional branches, only two are clearly observed in the data. The trajectories that correspond to these two branches at $\theta_f = 10°$ are plotted in Fig. 6 and discussed in Sec. V. In the simulated energy-θ plot in Fig. 12 the branch of the measured energy-θ plot at $E/E_0 \approx 0.18$ actually consists of two branches with nearly the same energies. Only one peak, and therefore one branch, is observed in the corresponding measured energy spectra [see Fig. 6(a)] due peak broadening by thermal vibrations and the limited resolution of the detector. The trajectory analysis indicates that both of these branches are due to the kinked zigzag trajectories, an example of which is plotted in Figs. 6(b) and 6(c). As can be seen in the simulated energy-θ plot, the kinked zigzag trajectories have a forward rainbow angle where the branches merge at $\theta_f = 15°$. Since the two branches are not resolved in the data the rainbow angle cannot be determined from the measured energy-θ plot, but it can be found by looking for a maximum in the intensity of the (KZZ) peak in the energy spectra as a function of θ_f. A broad maximum is indeed found in the data at $\theta_f = 20° \pm 5°$. The agreement between the measured and simulated rainbow angles for the kinked zigzag trajectories is rather good considering that these trajectories involve multiple large-scattering-angle collisions and, as a result, are very sensitive to the form of the potential. This rainbow is not observed in the simulations when the purely repulsive potential is used.

According to the trajectory analysis, the branch of the measured energy-θ plot at $E/E_0 \approx 0.06$ and $20° \leq \theta_f \leq 30°$ in Fig. 12 is primarily due to kinked chain trajectories similar to the one plotted in Fig. 6. Although there are several branches at about this energy in the simulated energy-θ plot, further analysis indicates that these other trajectory types have much lower scattering cross sections than the kinked chain trajectory at these final angles. The kinked chain peak is not clearly observed in the measured energy spectra for $\theta_f > 18°$. This may be due to the enhanced neutralization of these trajectories, as is discussed in a recent study.[47]

Since these low-energy features are due to complicated trajectories involving multiple large-scattering-angle collisions with the surface atoms, it might be expected that they make insignificant contributions to the scattered intensity. In fact, they have large scattering cross sections at certain final angles [see energy spectra in Fig. 6(a) and the corresponding discussion in the text].

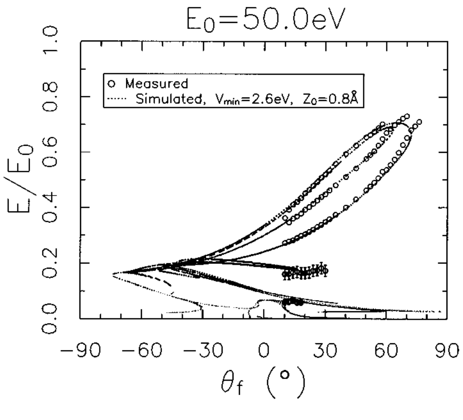

FIG. 12. Measured energy-θ plot for $E_0 = 50.0$ eV compared to a simulation using the total scattering potential (see Fig. 2). Branches with energies below the QS branch are observed in the simulations and data for $E_0 > 30$ eV, indicating new types of trajectories.

H. Data vs simulation, $E_0 = 100.6$ eV

In Fig. 13 measured and simulated energy-θ plots for $E_0 = 100.6$ eV are compared. The simulation, which uses the total potential, is in very good agreement with the data. As was the case at $E_0 = 50.0$ eV, there are two loops in the data corresponding to chain and zigzag scattering ($E/E_0 \geq 0.25$), but the QD and TZZ branches no longer have the same energy according to the simulation. The zigzag loop lies within the chain loop, with the QD branch at a larger E/E_0 than the TZZ branch for these θ_f. In the measured energy spectra the DZZ and TZZ peaks could not be reliably resolved, so the measured energy-θ plot has only three branches for ($E/E_0 \geq 0.25$).

There are two branches in the measured energy-θ plot for $E/E_0 < 0.25$. The simulation, in contrast, has many branches that contribute to the scattering at these energies. However, not all of these branches involve trajectories with large cross sections. According to the simulations the branch in the mea-

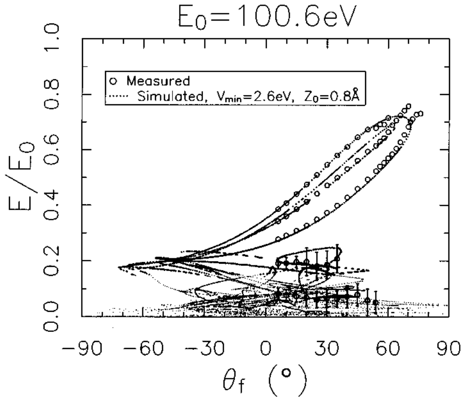

FIG. 13. Measured energy-θ plot for $E_0 = 100.6$ eV compared to a simulation using the total potential (see Fig. 2).

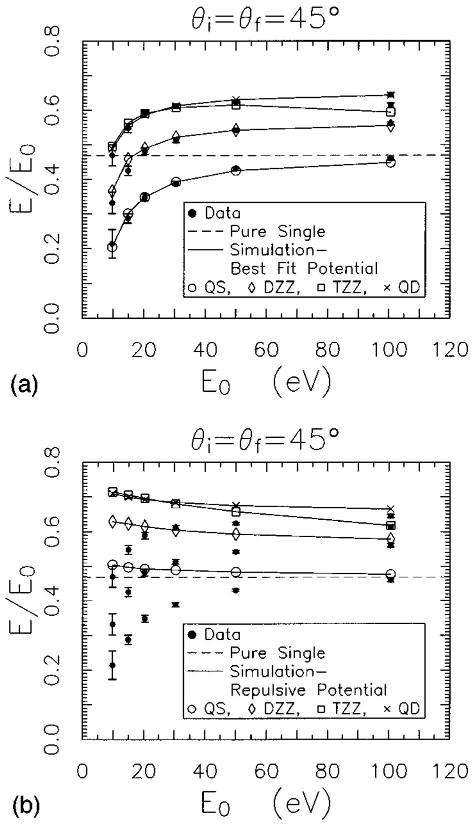

FIG. 14. (a) Measured fractional peak energies for the 90° specular scattering geometry as a function of E_0 (see Fig. 4 for energy spectra) compared to the peak energies from the simulations using the total potential (see Fig. 2). The kinematic factor for pure single scattering is also shown. (b) Same as (a), except that the data are compared to simulations using only the repulsive part of the potential.

sured energy-θ plot at $E/E_0 \approx 0.2$ is due to complicated trajectories involving top-layer atoms and the branch at $E/E_0 \approx 0.07$ is due to both complicated top-layer trajectories and trajectories that penetrate the top layer and scatter from second-layer atoms. These trajectories are similar to those that contribute to the $E_0 = 50.0$ eV energy-θ plot at low energies (see Fig. 6).

VII. DISCUSSION

In the preceding section we have shown that simulated energy-θ plots using the total interaction potential are in excellent agreement with the measured energy-θ plots for Na^+ scattered from Cu(001)⟨100⟩ with $\theta_i = 45°$ at incident energies ranging from 10 to 100 eV. Both the energy loss to the surface and the positions of the rainbow angles are sensitive to the attractive term in the interaction potential over this range of incident energies. At the lowest energies ($E_0 \leqslant 14.9$ eV) the forward rainbow is missing from the scattered flux due to trapping. In this section we discuss the relative roles that the attractive and repulsive parts of the ion-surface interaction play in determining the energy transfer to the surface, the positions of the forward rainbow angles, and trapping.

A. Energy loss vs E_0

Much can be learned about the scattering dynamics by examining how the energy spectra evolve as a function of E_0. Figure 4 shows a series of measured energy spectra at $\theta_i = \theta_f = 45°$ for $E_0 = 9.7$, 14.9, 20.3, 50.0, and 100.6 eV. As discussed in Sec. V, the three-peak structure and the trajectory assignments of the peaks remain essentially unchanged throughout this range of E_0. However, the relative heights, fractional energies, and fractional widths of the peaks change as a function of incident energy.

The change in the relative peak heights as a function of E_0 simply reflects the change in the relative scattering cross sections for the different types of trajectories: The relative cross section for multiple-scattering trajectories becomes smaller as the incident energy is increased. The fractional widths of the peaks increase as the incident energy is reduced due to an increased sensitivity to the thermal momentum fluctuations of the surface atoms.[9,26,48] The fractional widths of the peaks also grow with increasing surface temperature. A detailed analysis of this peak broadening is discussed elsewhere.[8]

The repulsive and attractive terms in the interaction potential influence the energy transfer to the surface in different ways. This can be understood by examining the energies and angles of the scattered ions as E_0 is varied. In Fig. 14(a) the measured (closed circles) fractional final energies E/E_0 of the peaks from Fig. 4 are plotted as a function of E_0 for $\theta_i = \theta_f = 45°$. The peak energies from an $E_0 = 30.4$ eV spectrum are also plotted. The fractional energies of the peaks from simulations using the total potential are also shown: the simulated QS, DZZ, TZZ, and QD energies are indicated by solid lines with open circles, open diamonds, open squares, and crosses, respectively. The simulations are in excellent agreement with the measured energy losses throughout the incident energy range. The dashed line indicates the kinematic factor ($E/E_0 = 0.47$) for a binary collision through $\theta_{\mathrm{TSA}} = 90°$. The fractional energy loss is independent of E_0 for such a collision. Figure 14(a) shows that the energies of the measured and simulated QS peaks lie below the kinematic factor for all E_0, with the difference increasing as E_0 is reduced. This trend is due to the increased influence of the image potential on the trajectories at low E_0. According to Eq. (4), the energy loss to the surface in a binary collision increases as a function of D/E_0, where D is the depth of the attractive well in the potential. The measured QS energy loss approaches the kinematic factor at $E_0 = 100$ eV, suggesting that the influence of the attractive well on the scattering becomes negligible for $E_0 > 100$ eV.

So far we have discussed only the influence of the attractive term in the potential on the energy transfer to the surface. The long-range tails of the repulsive potentials also influence the energy transfer, as illustrated in Fig. 14(b), where the measured fractional final peak energies as a function of E_0 for $\theta_i = \theta_f = 45°$ are compared with simulations using only the purely repulsive potential. As in Fig. 14(a), the results of the simulations are indicated by solid lines and the kinematic factor for a binary collision is indicated by a dashed line. The simulated fractional energy losses are in poor agreement with the data, especially for $E_0 \leqslant 50$ eV. In fact, the simulations predict that E/E_0 should increase as E_0 is reduced, in direct contradiction with both the data and the simulations using the total potential.

This trend is a result of multiple long-range scattering events. In the simulations using the purely repulsive potential, E/E_0 for the QS peak lies above the kinematic factor for all E_0. A detailed analysis of the simulated QS trajectories reveals that as the ion collides with its primary scattering partner it simultaneously undergoes small momentum transfer collisions with the nearest-neighbor surface atoms, which reduces the overall energy transfer to the surface. This is equivalent to increasing the effective mass of the primary scattering partner.

It is somewhat counterintuitive that increasing the number of scattering partners can reduce the energy transfer. Consider that an ion typically experiences long-range small-angle collisions with surface atoms before and after the primary collision in a QS trajectory. According to the kinematic factor [see Eqs. (2) and (3)] these small-angle scattering events result in inconsequential energy transfers, since $dk/d\theta_{\mathrm{TSA}}$ approaches 0 as θ_{TSA} approaches 0°. However, these events reduce θ_{TSA} in the *primary* collision and consequently the total-energy transfer decreases significantly for this collision, since $dk/d\theta_{\mathrm{TSA}}$ reaches a maximum at $\theta_{\mathrm{TSA}} = 90°$.[27] As we noted above, these long-range multiple-scattering effects essentially increase the effective mass of the surface atom. This increased effective mass, like the attractive well, has an increasing effect on the fractional energy transfer as E_0 is reduced.

Therefore, the final fractional energy in the experiments reflects a competition between the increased effective mass, which tends to increase E/E_0, and the attractive interaction, which tends to do the opposite. It is clear from the simulations in Fig. 14(a), which include both effects, that the attractive term produces the more important effect at these energies. Similar trends in E/E_0 might also be expected for other ions or reactive species scattering from metal surfaces, since there will be a strong attractive interaction between the surface and scatterer. In the scattering of neutral nonreactive species such as noble gases, however, the increased effective mass may dominate the energy transfer since the attractive well depth is typically $D \leqslant 100$ meV (compared to $D \approx 1-3$ eV for alkali ions).

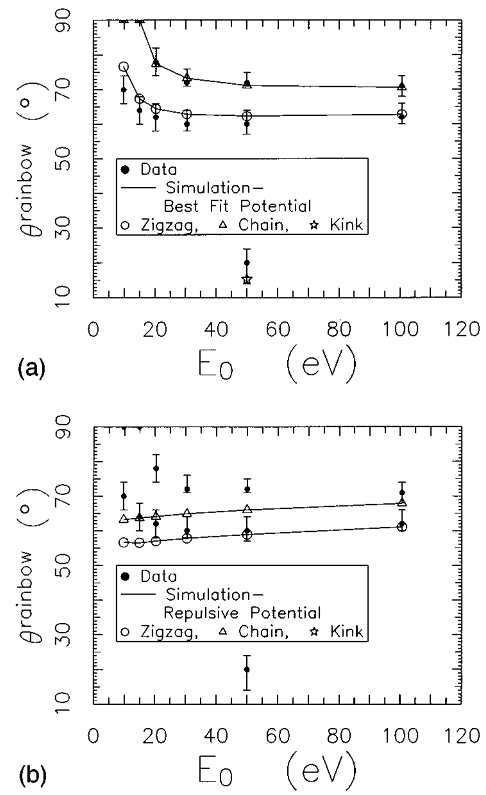

FIG. 15. (a) Measured rainbow angles as a function of E_0 compared to the rainbow angles from the simulations using the total potential. There are three types of rainbows shown: chain, zigzag, and kinked zigzag. The chain rainbows that are missing due to trapping are plotted at $\theta_f = 90°$. (b) Same as (a), except that the data are compared to simulations using only the repulsive part of the potential.

B. Rainbow angles vs E_0

The influence of the attractive interaction on the angular distributions of the scattered ions can be demonstrated by plotting the positions of the rainbow angles as a function of incident energy. We have done this in Figs. 15(a) and 15(b) for the rainbows identified from the energy-θ plots presented earlier in this paper. The closed circles represent the positions of the measured rainbow angles that are determined, when possible, by the angle at which the branches of the energy-θ plots merge. When the branches are not resolvable the rainbow angle is determined from the position of the peak in the angular intensity distribution. There are three different types of rainbows observed in the data for 9.7 eV$\leqslant E_0 \leqslant$100.6 eV. The forward zigzag rainbow was observed for all E_0. The forward chain rainbow is missing for $E_0 \leqslant 14.9$ eV due to trapping in the attractive well, but is present at all other energies. The rainbow due to the kinked zigzag trajectories, however, is only observed at $E_0 = 50.0$ eV.

The simulated rainbow positions using the total potential and the purely repulsive potential are compared to the data in Figs. 15(a) and 15(b), respectively. The points corresponding to the simulated chain rainbow positions are marked with open triangles connected by lines, the zigzag rainbow positions are marked by open circles connected by lines, and the kinked zigzag rainbow at $E_0 = 50.0$ eV is marked by an open star. As the incident energy is reduced from 100 to 10 eV, the chain and zigzag rainbow angles shift in the simulations, with the direction of the shift depending on whether or not the attractive well is included in the potential. For example, in the simulations using the purely repulsive potential the zigzag rainbow angle *decreases* from 61.1° to 56.6° as the incident energy is reduced from 100.6 to 9.7 eV, whereas when the total potential is used, the zigzag rainbow angle first *decreases* about 0.5° between 100.6 and 50.0 eV and then *increases* from 62.3° to 76.7° as E_0 is reduced from 50.0 to 9.7 eV.

The difference in the energy dependence of the rainbow angles in Figs. 15(a) and 15(b) reflects the competition between two effects:[49] the diminished corrugation of the surface at lower incident energies, which tends to shift the rainbows towards the surface normal (i.e., to smaller θ_f), and the increasing degree of trajectory bending in the attractive well, which tends to shift the rainbow angle away from the surface normal. In the simulations using the purely repulsive potential, only the change in surface corrugation effects the position of the rainbow angles, so the rainbow angles shift towards the surface normal as the incident energy is reduced. However, in the simulations using the total potential both the decreased corrugation and the increasing importance of the attractive well influence the rainbow angles. As seen in Fig. 15(a), the rainbow angles shift away from the surface normal when the incident energy is reduced from 50 to 9.7 eV, which indicates that the attractive well influences the shift in the rainbow angles more than the change in surface corrugation. At higher energies the influence of the attractive well becomes negligible and the energy dependence of the surface corrugation dominates the shifts in the rainbow angles. This results in a slight decrease in the measured zigzag rainbow angle as the incident energy is decreased from 100 to 50 eV.

The simulations that include the attractive interaction reproduce the important trends and features in the data as the incident energy is varied: the shifts in the rainbow angles as a function of E_0, the missing chain rainbow at $E_0 \leqslant 14.9$ eV indicating trapping (plotted as $\theta^{\text{rainbow}}=90°$ in Fig. 15), and the presence of the kinked zigzag rainbow in the 50.0-eV data. In the simulations using the purely repulsive potential the kinked zigzag rainbow at 50.0 eV is missing and the chain and zigzag rainbows are in poor agreement with the data. This is particularly noticeable for $E_0 < 50$ eV, where the trajectory bending in the attractive well is most pronounced.

C. Interaction potential and simulations

The parametrization of the total ion-surface interaction potential $V_{\text{min}}=2.6$ eV and $z_0=0.8$ Å [see Eq. (1) and Fig. 2] was determined by comparing, for a range of E_0, the measured energy-θ plots to simulations in which these parameters were varied. These fit parameters are associated with the attractive term in the interaction potential. There are no adjustable parameters associated with the repulsive part of the potential (see the Appendix for a detailed discussion of the calculation of the repulsive potential).

The attractive term in the potential is a function of z, the distance from the top layer of surface atoms. It has the classical $1/4z$ image form far from the surface, saturates to a constant value (V_{min}) close ($z \leqslant z_0$) to the surface, and interpolates smoothly between the two limits at intermediate distances. The simulations using parametrizations close to the best-fit values are in the best agreement with the data. However, since there are error bars on the energy losses (about ±0.5 eV) and rainbow angles (about ±2°–3°) in the data, there is a range of parametrizations that is consistent with the data. Consequently, despite the sensitivity of the scattering distributions to the attractive term for $E_0 \leqslant 50$ eV, it is not possible to determine with certainty the depth or shape of the attractive well in the total ion-surface interaction potential (see Fig. 2).

For example, the best-fit potential has a well depth $D=1.5$ eV above the on-top site. Simulations using a parametrization $V_{\text{min}}=2.6$ eV and $z_0=2.5$ Å also agree with the measured energy-θ plots within the experimental uncertainty for all E_0. This is somewhat surprising since $D=2.5$ eV for this parametrization, and we argued in Sec. V that the energy transfer to the surface should increase monotonically with D/E_0. Although these two potentials have well depths that differ by 1 eV, simulations using both parametrizations predict the same energy loss for the QS peak, $E/E_0=0.35$, for $E_0=20.3$ eV scattering at $\theta_i=\theta_f=45°$. Evidently, the simple argument presented in Sec. V is not adequate.

The simple argument for the increased energy loss in the presence of the attractive well assumes that the ion is first accelerated towards the surface by the attractive well, that it *subsequently* collides with the surface, transferring momentum and energy to the surface atom, and that *afterward* it is decelerated (by the same attractive well that initially accelerated it) as it leaves the surface. In other words, it assumes that the attractive and repulsive forces act sequentially, not simultaneously. In the simulations the ion experiences an attractive force for $z > z_0$. Therefore the simple model should be satisfactory when z_0 is larger than the range of the repulsive potential. It is clear from Fig. 2 that this criterion is almost met when $z_0=2.5$ Å, but that it is not satisfied for the best-fit interaction potential ($z_0=0.8$ Å).

In the simulations using the best-fit total potential the attractive and repulsive forces act simultaneously, which increases the energy loss beyond that expected from the simple model. The ion experiences the attractive force due to the image interaction with the conduction electrons *while* it is colliding with the surface atom. A detailed trajectory analysis using the simulations indicates that this results in additional energy transfer to the surface atom during the collision. Therefore the energy transfer for the two different potential parametrizations is the same even though D is 1 eV smaller for the best-fit parametrization, i.e., the two parametrizations yield the same dynamics but different statics.

Potential parametrizations featuring attractive wells such that 1.3 eV$\leqslant D \leqslant$2.6 eV for the on-top site and 1.5 eV$\leqslant D \leqslant$2.6 eV for the hollow site have been found that produce simulated scattering distributions that fall within the error bars of the measured energy-θ plots. In comparison, in the best-fit total potential $D=1.5$ eV for the on-top site and $D=1.7$ eV for the hollow site [directly above a second-layer atom; see Fig. 1(a)]. Therefore, these results constrain the depth and the shape of the attractive well in the Na^+-Cu(001) interaction potential.

Some caution must be taken in associating the well depths determined from scattering experiments at these energies with chemisorption energies. The scattering ions experience a different potential than a chemisorbed species, since the recoiling surface atoms undergo significant displacements (typically ≈ 1 Å) during the collisions. We do note, however, that well depths for alkalis interacting with other metal surfaces have been measured by hyperthermal energy atom scattering at elevated temperatures[50,51] and field emission,[52] yielding values similar to those we report here.

The repulsive part of the potential used in this study is constructed from a sum of HF $(\mathrm{Na}\text{-}\mathrm{Cu})^+$ pair potentials (see the Appendix). A previous study on a similar system concluded that the ion-surface repulsion in the hollow site is underestimated using the sum of pair potentials approximation.[20,23] We checked for the validity of this approximation in our system by comparing the sum of pair potentials to a cluster calculation and found that the two calculations are in excellent agreement in the hollow site (see the Appendix). Further evidence that the sum of pair potentials approximation is sufficient is provided by the agreement between the low-energy branches of the simulated and measured energy-θ plots at $E_0 = 50.0$ and 100.6 eV, since these branches correspond to kinked trajectories that probe the hollow site (see Fig. 6).

D. Trapping

The chain rainbows in both the data and the simulations using the total potential are missing for $E_0 \leqslant 14.9$ eV. This is indicated by the gaps in the measured and simulated energy-θ plots at $\theta_f = 90°$ and can be attributed to the trapping of the *forward-scattered* ions in the attractive well of the ion-surface interaction potential. The simulations indicate that trapping can also occur for the backscattered ion flux. For example, in the simulation using the total potential for $E_0 = 9.7$ eV [see Fig. 9(b)] there is a gap indicating trapping at $\theta_f = -90°$ and $E/E_0 \approx 0.055$ in addition to the gap at $\theta_f = 90°$ and $E/E_0 = 0.37-0.58$.

According to the simulation at $E_0 = 9.7$ eV, the in-plane trajectories that scatter in the forward direction and are trapped actually have a kinetic energy as large as 5.8 eV at their turning point (the point farthest from the surface after the initial collision, where $P_z = 0$ momentarily), but do not escape the attractive well ($D = 1.5$ eV for the on-top site) because only a small component of the ion's velocity is directed perpendicular to the surface. These trajectories may be expected to skip along the surface for long distances before either coming to rest or subsequently scattering, perhaps from a defect.[1,53] This skipping motion has been reported for $E_0 = 200-2000$ eV Si scattering from Cu(111) at glancing angles.[53] Conversely, the in-plane trajectories that scatter in the backward direction and trap lose a large fraction of their incident energy in the initial collision with the surface. As a result, they have a much smaller total energy and are not likely to travel as far from the initial impact site. It is important to note that although the energy-θ plots presented here are restricted to in-plane scattering geometries, these conclusions are also generally valid for the out-of-plane scattering. For instance, the simulations indicate that the out-of-plane trajectories that trap at $E_0 = 9.7$ eV include both high-total-kinetic-energy forward-scattered trajectories and low-energy backscattered trajectories. In the case of these out-of-plane trajectories, we define forward-scattered trajectories as those having a component of momentum in the $\langle 100 \rangle$ direction that is parallel to the incident beam and the backscattered as those having a component that is antiparallel.

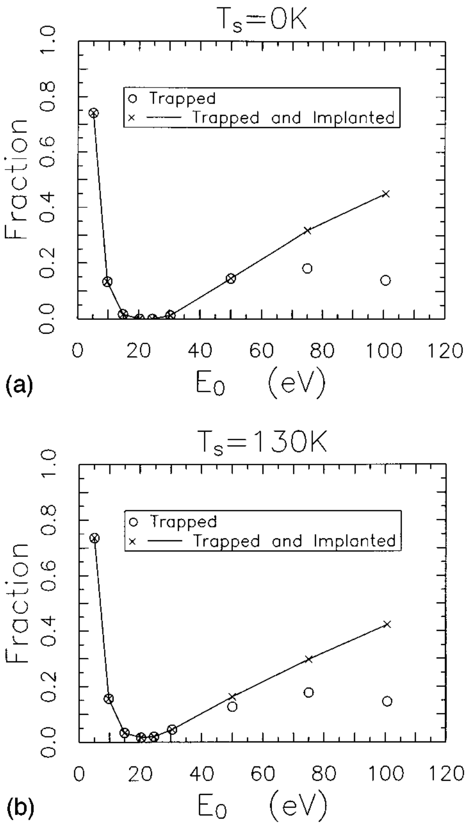

FIG. 16. (a) Trapped and implanted fractions for $\theta_i = 45°$ and $T_s = 0$ K as a function of E_0 according to simulations using the total potential. Zero-point motion is not included in the simulation. (b) Same as (a), except at $T_s = 130$ K, which corresponds to the experimental temperature.

Although the simulation correctly predicts that the gaps at $\theta_f = 90°$ should begin to appear in the chain energy-θ loop at incident energies between 20.3 and 14.9 eV for this system [Na^+ scattering in-plane from Cu(001)$\langle 100 \rangle$ with $\theta_i = 45°$], there is a limit to how accurately it can predict the trapped fraction. There are several reasons for this. In order for the simulation to predict the trapped fraction it must correctly determine the ultimate fate of the initially trapped trajectory, i.e., whether it subsequently escapes the attractive well or eventually comes to rest on the surface. This fate may be sensitive to factors such as surface defects, thermal vibrations, charge transfer, and the details of the interaction potential. The SAFARI simulations do not include charge transfer or surface defects. In addition, the simulations use a very simple model of the surface dynamics and there are uncertainties in the shape and depth of the attractive well.

Despite these shortcomings in the model, it is still instructive to consider the trapping fraction predicted by SAFARI. The simulations can provide a qualitative, if not quantitative, understanding of the dependence of the trapping fraction on the incident energy. They can also provide a detailed account of the trapping mechanisms. We will first discuss the predictions of the simulations regarding the trapping and then discuss how the limitations effect our results (see Ref. 10 for a more detailed discussion). In Fig. 16(a) the fraction of the trajectories that are trapped and implanted are plotted as a function of incident energy for $\theta_i = 45°$ and a vibration-free surface. In Fig. 16(b) the fractions are plotted for a $T_s = 130$ K surface. The simulations include out-of-plane trajectories and use the total potential.

A trajectory is considered implanted in the simulations if either the ion penetrates more than 7.22 Å below the top-layer plane of atoms (the atomic planes are separated by 1.805 Å) or the total energy of the ion drops below a minimum energy E_{min} while it is located below the top layer of atoms. In these simulations $E_{\mathrm{min}} = -1.0$ eV. The ions are considered trapped if the total energy of the ion drops below E_{min} while the ion is located above the top layer. The value of E_{min} is low enough to ensure that if an ion is labeled trapped it is not likely to subsequently escape, but not so small that it allows the simulation to run indefinitely. In all cases the trajectory calculation stops well before thermal equilibrium is reached. We also note that in the simulations the vast majority of ions that do not either trap or implant are scattered after their first encounter with the surface, although some do eventually scatter after initially trapping with $E > E_{\mathrm{min}}$.

According to Fig. 16(a), the fraction of ions that trap decreases dramatically as the incident energy is increased from 5 to 10 eV, becomes 0 between 15 and 30 eV, and then begins to increase again above 30 eV. The implanted fraction is 0 below $E_0 = 50$ eV and starts to increase between 50 and 75 eV. The relative fraction of ions that trap and implant is rather sensitive to the value of E_{min} and therefore the distinction between them is somewhat arbitrary in the simulations. According to Fig. 16(b), the most significant difference introduced by the surface vibrations is that, for a vibration-free surface, there is no trapping or implanting for 20 eV$\leq E_0 \leq$25 eV, whereas there is a small probability of trapping at these energies at $T_s = 130$ K. As we discuss below, most of this additional trapping is from the backscattered trajectories.

The nonzero trapping fraction for 20 eV$\leq E_0 \leq$25 eV predicted by the $T_s = 130$ K simulations is consistent with the experimental observation that, at these energies, the intensities of the measured energy spectra decrease as the surface is dosed by the beam. This intensity drop is attributable to trapped Na that shifts the surface work function resulting in an increase in the rate of neutralization of the scattered flux.[11]

The simulations indicate that the trajectories that lead to trapping for $E_0 \leq 14.9$ eV are significantly different from those that contribute to the trapping for $E_0 \geq 30$ eV. At the lower energies the trapped trajectories are similar to those shown in Figs. 3(b) and 3(c) and involve total-energy transfers of less than 14 eV to the 1–3 atoms involved in the scattering. Above 30 eV, however, the trajectories that trap are similar to those shown in Figs. 6(b) and 6(c) for $E_0 = 50.0$ eV. These trapped trajectories involve very large energy transfers ($E/E_0 \lesssim 0.05$) to a few (typically 2–4) surface atoms adjacent to the impact site. For example, at $E_0 = 50.0$ eV some of the trapping comes from the branch of the energy-θ plot located at $\theta_f = 90°$ and $E/E_0 \approx 0.025$ in Fig. 12. These trajectories transfer ≈48.7 eV to just a few surface atoms before trapping. As a result, surface defects may be formed and local heating may occur. It has been postulated that local heating during trapping may be an important step in thin-film growth using hyperthermal energy beams.[1]

Simulations also indicate that, in general, the backscattered features ($\theta_f < 0°$) in the energy-θ plots, including gaps indicating trapping at $\theta_f = -90°$, are much more sensitive than the forward-scattered features to the thermal vibrations of the surface atoms, the treatment of the surface dynamics, and the ion-surface interaction potential.[10,28,46] In Fig. 16, for example, the trapped fraction increases from 0% to 2% when the thermal vibrations are included at $E_0 = 20.3$ eV. According to the vibration-free simulation of in-plane scattering there is a rainbow at $\theta_f \approx -78°$ [see Fig. 8(b)] and there is no in-plane scattering for $-90° < \theta_f < -78°$. In contrast, when the simulation is repeated for a $T_s = 130$ K surface, the in-plane intensity extends back to $\theta_f \approx -90°$. Furthermore, the simulation, which includes out-of-plane scattering, indicates that essentially all of the trapped trajectories are backscattered ($\theta_f = -90°$). We have also used the $E_0 = 20.3$ eV simulations to estimate the sensitivity of the trapped fraction to how the surface dynamics are treated. When the vibration-free simulation described above is repeated without including the nearest-neighbor forces between surface atoms [i.e., free atoms located at the Cu(001) equilibrium positions], the backscattering is again found to extend to $\theta_f = -90°$ and some of the trajectories are trapped. Similar results are found when small changes are made to the repulsive term in the interaction potential. Therefore, although the backscattered features are very sensitive to small variations in the surface temperature, surface dynamics, and interaction potential, the trapping fraction predicted by the simulations only changes modestly.

The simulations do not include surface defects, such as steps, which may result in collisions that transfer enough of the trapped ion's momentum parallel to the surface into momentum perpendicular to the surface for it to escape.[53] Therefore, it is difficult to estimate how much this mechanism influences the trapping fraction. The surface corrugation may also convert parallel to perpendicular momentum and scatter the initially trapped trajectories. The simulations indicate, however, that this type of process does not influence the trapped fraction significantly since most of the trajectories that initially trap never escape the surface.

Some fraction of the ions that are initially trapped after striking the surface may subsequently neutralize by resonant electron transfer from the surface into the ionization level.[40] In such an event the newly formed neutral atom may escape, since it no longer experiences the strong image attraction to the surface. The neutralization probability may be large enough to exert a considerable influence on the trapped fraction. For example, measurements of the neutralization probability have been recently reported for $E_0 = 5$ eV Na^+ incident on Cu(001)⟨100⟩ at $\theta_i = 45°$ and scattered at $\theta_f = 45°$. The neutralization probability is about 10% under these conditions and tends to increase as the incident energy is reduced.[40] This effect may be even more pronounced for the trapping at $E_0 \geq 30$ eV in Fig. 16. The neutralization probability of the lowest-energy peak in Fig. 6(a) ($E_0 = 50.0$ eV, $\theta_f = 10°$, and $E/E_0 = 0.065$), which is comprised of trajectories similar to those that trap for $E_0 \geq 30$ eV, is about

50%.[10,47] Therefore, the simulations would have to properly account for neutralization in order to quantitatively predict the trapping fraction.

VIII. CONCLUSION

In this paper we have presented a study of the dynamics of hyperthermal Na^+ scattering from Cu(001)⟨100⟩ at an incident angle of 45°. In particular, we have discussed the energy transfer, trapping, and the influence of the interaction potential on the dynamics. Using a classical trajectory simulation with a model potential, we achieved excellent agreement between measured and simulated scattering distributions for 10–100 eV Na^+ scattering from Cu(001). We have demonstrated that, for sufficiently low incident energies, the trajectories, and consequently the scattered energy and angular distributions, are very sensitive to the attractive term of the ion-surface potential. In particular, we found that it is necessary to include the attractive interaction in the simulations in order to reproduce the measured energy loss and the measured forward rainbow angles for incident energies below 100 eV.

It has been shown that the attractive term increases the energy loss of the scattered ions to the surface and moves the forward rainbow angles further from the surface normal and that these two effects become more pronounced as the incident energy is reduced. The importance of the attractive well was most clearly demonstrated in the $E_0 = 9.7$ and 14.9 eV scattering, where both the simulated and measured energy-θ plots had gaps in the chain loops at $\theta_f = 90°$, indicating trapping of the scattered ions in the attractive well. Using the simulations, we have discussed in detail the mechanism of energy transfer in the presence of the attractive well and the mechanisms that lead to trapping at hyperthermal energies.

For $E_0 = 9.7$, 14.9, 20.3, 30.4, 50.0, and 100.6 eV scattering we found good quantitative agreement between measured and simulated energy-θ plots using the best-fit parametrization of the potential ($V_{\mathrm{min}} = 2.6$ eV and $z_0 = 0.8$ Å). We expect similar agreement for energies at least as high as $E_0 = 400$ eV. This best-fit total potential features an attractive well with a depth of 1.5 eV for the on-top site and 1.7 eV for the hollow site. The scattering is, however, relatively insensitive the shape and depth of the attractive well in the interaction potential, since simulated energy-θ plots agree reasonably well with the data for a range of parametrizations (V_{min}, z_0) of the attractive term in the potential. Well depths ranging from 1.3 to 2.6 eV for the on-top site and 1.5–2.6 eV for the hollow site produced simulations in agreement with the data within the experimental error. We have discussed, in terms of our model for the interaction potential, how the energy transfer could be similar for two parametrizations with well depths near the ends of this range.

We have qualitatively discussed the trends in the trapping probability as a function of E_0 predicted by the simulations. According to these simulations there is a minimum in the trapping probability for incident energies between 15 and 30 eV and the trajectories that lead to the trapping at low incident energy differ from those at higher energies. In particular, at the higher energies the ions lose a very large fraction of their energy in the initial collision to just a few surface atoms near the impact site. As a result, surface defects may form and local heating may occur. These are both processes that may be important in low-energy ion thin-film deposition.

ACKNOWLEDGMENTS

The authors gratefully acknowledge David Goodstein for useful discussions and assistance with this manuscript. We would also like to thank Ernie Behringer, David Adler, Eugene Zaremba, and Steven Holloway for helpful discussions. This work has been supported by the National Science Foundation (Grants Nos. NSF-DMR-9007799 and DMR-9313818). Additional support for the research came from the Cornell Materials Science Center (Grant No. NSF-DMR-9121654) and from the Air Force Office of Scientific Research (Grants Nos. AFOSR-91-0137 and F49620-93-1-0504).

APPENDIX

In this appendix we discuss the details of the calculation of the repulsive term in the potential and demonstrate that the sum of pair potentials approximation is valid for this system. The sum of pair potentials that is used to model the repulsive part of the ion-surface interaction potential runs over the n surface atoms nearest the ion at any point in its trajectory, where typically $n \geqslant 6$. The value of n is determined by varying it until the trajectory converges. The $(\mathrm{Na\text{-}Cu})^+$ pair potentials are calculated using the Hartree-Fock self-consistent-field code in the quantum chemistry package GAUSSIAN 88.[54] The pair potential is calculated by subtracting the energies of the isolated Cu and Na^+, also calculated using the HF code, from the energy of the charged $(\mathrm{Na\text{-}Cu})^+$ dimer, i.e., as a function of separation r, $V^{\mathrm{pair}}(r) = E[(\mathrm{Na\text{-}Cu})^+, r] - E(\mathrm{Na}^+) - E(\mathrm{Cu})$. As expected, since Cu has a larger ionization potential than Na, at large r the dimer calculation predicts that the Cu atom is neutral and the Na is singly charged Na^+.

Large uncontracted Gaussian-type orbital basis sets are used to allow a more accurate description of the distortion of the electron orbitals at the small Na-Cu separations ($\gtrsim 0.6$ Å) required in these scattering calculations. The Gaussian basis sets used are taken from the compilation by Poirier, Kari, and Csizmadia, using a $(14s,9p,5d)$ basis set for Cu and a $(10s,4p)$ basis set for Na.[55] In order to better allow for atomic polarization, these basis sets were augmented with diffuse polarization functions. The diffuse polarization functions, $(2p)$ for Cu, $(2d)$ for Na^+, and $(2p)$ and $(2d)$ for neutral Na, are taken from the compilation by Huzinaga.[56] All calculations consider spin-up and down electrons independently (i.e., they are spin unrestricted). The resulting potential has been compared with others calculated using smaller basis sets[55] and/or different Hartree-Fock computational packages and it is generally in agreement with the best of these other potentials to within a few tenths of an eV. The calculated electronic configurations of the isolated atoms are found to conform to experimental electronic configurations reported in the literature, in particular the Cu configuration is Cu $1S$ $(3d10\ 4s1)$ rather than Cu $1D$ $(3d9\ 4s2)$.

The pair potential $V^{\mathrm{pair}}(r)$ is plotted in Fig. 17 for a range of separations. This potential features a strong repulsive interaction due to the Pauli repulsion at small separations and a

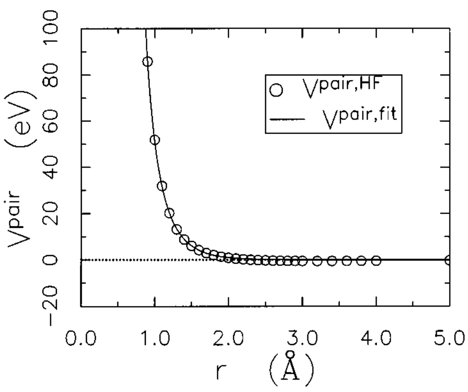

FIG. 17. Comparison of the Hartree-Fock (HF) $(\text{Na-Cu})^+$ pair potential and the double exponential fit that is used to generate the repulsive part of the potential in our classical trajectory simulations.

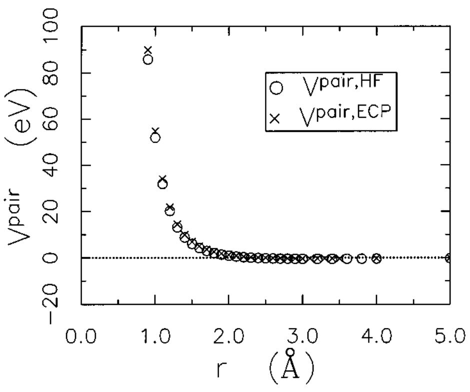

FIG. 19. Hartree-Fock $(\text{Na-Cu})^+$ pair potential calculated with the full basis set compared to a Hartree-Fock pair potential calculated with an effective core potential (ECP); see the text.

shallow well at larger separations due to the induced dipole on the Cu. Since the formation of the image charge on a surface involves a many-body interaction between the ion and the conduction electrons that cannot be accounted for in the HF pair calculation, the scattering simulations use a pair potential with no attractive well that is obtained by fitting the repulsive wall of the HF pair potential with a sum of two exponentials. The image interaction is, however, included in the *total* ion-surface potential by adding an additional z-dependent term to the sum of pair potentials (see Fig. 2). The actual pair potential used in the simulations has the form $V^{\mathrm{pair}}(r)=Ae^{-Br}+Ce^{-Dr}$, where $A=1336$ eV, $C=55\,200$ eV, $B=3.623$ Å^{-1}, and $D=8.184$ Å^{-1}. As shown in Fig. 17, the double exponential fit reproduces the HF calculation well for the separations and energies of interest: $1.0\ \text{Å}\leqslant r\leqslant 2.1\ \text{Å}$ and $0\ \text{eV}\leqslant V^{\mathrm{pair}}(r)\leqslant 100$ eV.

In the calculation of the pair potential it is assumed that a charged $(\text{Na-Cu})^+$ dimer best represents the interaction potential between the sodium ion and a Cu surface atom for the range of separations of interest. However, as Na^+ approaches the surface, its image charge becomes localized very near the ion. Charge transfer may also occur, resulting in neutralized Na. Therefore, it is instructive to compare the $(\text{Na-Cu})^+$ pair potential above to a similar calculation for a neutral (Na-Cu) dimer (see Fig. 18). As can be seen in Fig. 18, the repulsive parts of the (Na-Cu) and $(\text{Na-Cu})^+$ pair potentials are similar, but the attractive wells differ. In contrast to the $(\text{Na-Cu})^+$ case, the attractive well in the (Na-Cu) pair potential can be attributed to the bonding of the outer s orbitals. Since the pair potentials used in the simulations were fit to only the repulsive walls of the HF pair potentials, which were insensitive to the charge state, we conclude that the choice of the charge state of the dimer used to calculate the potential [i.e., $(\text{Na-Cu})^+$] does not affect the results of the scattering simulation significantly. It should be noted that this may not hold for ions or surfaces with very different electronic structures.

We noted earlier that constructing the repulsive term in the interaction potential from a sum of pair potentials failed in a study of 10–100 eV K^+ scattering from W(110), where it was concluded that it was necessary to include an additional hollow site repulsion in the potential.[20,23,24] In order to verify that this approximation is valid for Na^+ scattering from Cu(001), we performed a cluster calculation of the interaction potential for Na^+ directly above the hollow site and compared it with that calculated from a sum of pair potentials. In the cluster calculation the surface is represented by a cluster of five Cu atoms that included the second-layer Cu directly below the hollow site and the four top-layer Cu at-

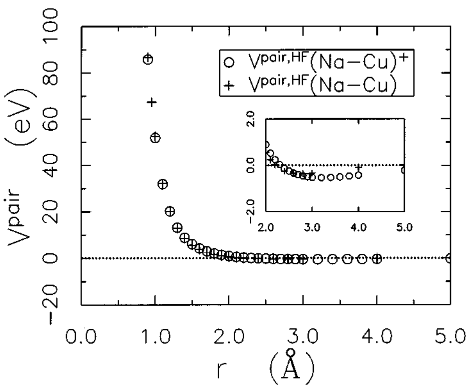

FIG. 18. Comparison of the Hartree-Fock potential energies for both $(\text{Na-Cu})^+$ and the (Na-Cu) neutral dimers. The region near the attractive well is detailed in the inset. The repulsive part of the potential, which is used in the simulations, is not sensitive to the charge state of the dimer.

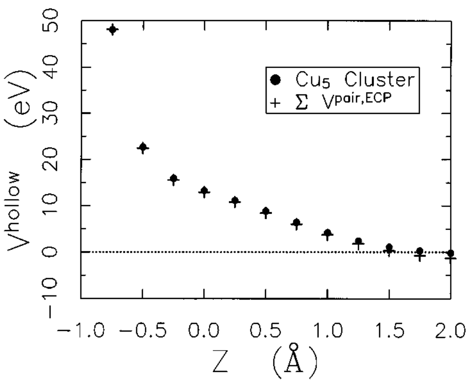

FIG. 20. Sum of Hartree-Fock $(\text{Na-Cu})^+$ pair potentials compared to a NaCu_5 cluster calculation as a function of distance above the hollow site in the Cu(001) surface [directly above a second-layer atom; see Fig. 1(a)]. The effective core potential was used in both calculations and $z=0$ corresponds to the top layer of atoms.

oms adjacent to the hollow site [see Fig. 1(a)]. This cluster size should be sufficient to reveal any many-body effects at short range where repulsive interactions dominate, although it would not be expected to accurately represent the long-range image attraction.[57]

In order to make this problem computationally tractable, it is necessary to reduce the degrees of freedom by replacing the core electrons of the Cu atoms with an effective core potential (ECP). However, since scattering in this energy range results in relatively small ion-surface atom separations, it is important to include explicitly more than the $4s$ electron on the Cu. For this we use an ECP and the accompanying basis set generated by Wadt and Hay.[58] The ECP replaces the innermost ten electrons and the remaining electrons are described by a contracted $(5s,4p,4d)$ basis set consisting of $5s$, $5p$, and $5d$ primitive Gaussians. For the Na a contracted $(4s,2p)$ basis set with $17s$ and $8p$ primitives is taken from Ref. 55 and augmented with the same $2d$ diffuse polarization functions as above.

In order to facilitate the comparison between the cluster and the sum of pair potential calculations, the ECP basis sets were used to recalculate the (Na-Cu)$^+$ pair potential. As can be seen in Fig. 19, the result is in good agreement with the (Na-Cu)$^+$ pair potential calculated with the larger basis sets. In Fig. 20 the results of the calculation for Na over the hollow site of the Cu$_5$ cluster are compared with a sum of pair potentials; both calculations use the same ECP basis set, and in the cluster calculation the zero of the potential is defined as the sum of the HF energies of the isolated Na$^+$ and the Cu$_5$ cluster. The two calculations agree to within $\frac{1}{3}$ eV for heights $z<0.8$ Å above the surface. For larger z, the sum of pair potential falls below the cluster potential by an amount comparable to the attractive wells from the pair potentials. Since only the repulsive walls of the pair potentials are represented in the scattering simulations this disagreement is not expected to effect the simulations. The agreement between the cluster potential and sum of pair potentials may not hold for atoms with different electronic structures.[24]

---

*Present address: Xerox Corporation, 114-22D, 800 Phillips Road, Webster, NY 14580.

†Present address: Lawrence Livermore National Laboratory, L-482, P.O. Box 808, Livermore, CA 94551.

[1] B. W. Dodson, Phys. Rev. B **36**, 1068 (1987).

[2] H. P. Kaukonen and R. M. Nieminen, Phys. Rev. Lett. **68**, 620 (1992).

[3] S. R. Kasi, H. Kang, C. S. Sass, and J. W. Rabalais, **10**, 1 (1989).

[4] B. H. Cooper and E. R. Behringer, in *Low Energy Ion-Surface Interactions, Advances in Ion Chemistry and Physics,* edited by J. Wayne Rabalais (Wiley, Sussex, 1994).

[5] D. R. Peale, D. L. Adler, B. R. Litt, and B. H. Cooper, Rev. Sci. Instrum. **60**, 730 (1989).

[6] D. L. Adler and B. H. Cooper, Rev. Sci. Instrum. **59**, 137 (1988).

[7] R. L. McEachern, D. L. Adler, D. M. Goodstein, G. A. Kimmel, B. R. Litt, D. R. Peale, and B. H. Cooper, Rev. Sci. Instrum. **59**, 2560 (1988).

[8] C. A. DiRubio, D. M. Goodstein, B. H. Cooper, and K. Burke, Phys. Rev. Lett. **73**, 2768 (1994).

[9] D. M. Goodstein, C. A. DiRubio, B. H. Cooper, and K. Burke, Phys. Rev. Lett. **1**, 175 (1994).

[10] C. A. DiRubio, Ph.D. thesis, Cornell University, 1993 (unpublished).

[11] G. A. Kimmel, D. M. Goodstein, Z. H. Levine, and B. H. Cooper, Phys. Rev. B **43**, 9403 (1991).

[12] D. M. Goodstein, S. A. Langer, and B. H. Cooper, J. Vac. Sci. Technol. A **6**, 703 (1988).

[13] D. M. Goodstein, R. L. McEachern, and B. H. Cooper, Phys. Rev. B **39**, 13 129 (1989).

[14] R. Brako and D. M. Newns, Rep. Prog. Phys. **52**, 655 (1989).

[15] J. E. Inglesfield, Surf. Sci. **127**, 555 (1983).

[16] P. M. Echenique, R. M. Nieminen, J. C. Ashley, and R. H. Ritchie, Phys. Rev. A **33**, 897 (1986).

[17] F. Sols, P. Miranzo, and F. Flores, Surf. Sci. **161**, 33 (1985).

[18] J. B. Marston, D. R. Andersson, E. R. Behringer, B. H. Cooper, C. A. DiRubio, G. A. Kimmel, and C. Richardson, Phys. Rev. B **48**, 7809 (1993).

[19] M. J. Puska and R. M. Nieminen, Phys. Rev. B **27**, 6121 (1983).

[20] A. D. Tenner, R. P. Saxon, K. J. Gillen, D. E. Harrison, Jr., T. C. M. Horn, and A. W. Kleyn, Surf. Sci. **172**, 121 (1986).

[21] A. D. Tenner, K. T. Gillen, T. C. M. Horn, J. Los, and A. W. Kleyn, Surf. Sci. **172**, 90 (1986).

[22] A. D. Tenner, K. T. Gillen, and A. W. Kleyn, NIM Phys. Rev. B **17**, 108 (1986).

[23] A. D. Tenner, K. T. Gillen, T. C. M. Horn, J. Los, and A. W. Kleyn, Phys. Rev. Lett. **52**, 2183 (1984).

[24] P. J. van den Hoek, A. D. Tenner, A. W. Kleyn, and E. J. Baerends, Phys. Rev. B **34**, 5030 (1986).

[25] T. C. M. Horn, Pan Haochang, P. J. van den Hoek, and A. W. Kleyn, Surf. Sci. **201**, 573 (1988).

[26] R. L. McEachern, Ph.D. thesis, Cornell University, 1989 (unpublished).

[27] R. L. McEachern, D. M. Goodstein, and B. H. Cooper, Phys. Rev. B **39**, 10 503 (1989).

[28] D. L. Adler and B. H. Cooper, Phys. Rev. B **43**, 3876 (1991).

[29] J. P. Biersack and J. F. Ziegler, in *Ion Implantation Techniques*, edited by H. Ryssel and H. Glawischnig, Springer Series in Electrophysics Vol. 10 (Springer-Verlag, Berlin, 1982).

[30] E. Hulpke, Surf. Sci. **52**, 615 (1975).

[31] E. Hulpke and K. Mann, Surf. Sci. **133**, 171 (1983).

[32] S. R. Kasi, M. A. Kilburn, H. Kang, and J. W. Rabalais, J. Chem. Phys. **88**, 5902 (1988).

[33] H. Akazawa and Y. Murata, J. Chem. Phys. **92**, 5551 (1990).

[34] B. H. Cooper, C. A. DiRubio, G. A. Kimmel, and R. L. McEachern, Nucl. Instrum. Methods Phys. Res. Sect. B **64**, 49 (1992).

[35] N. D. Lang and W. Kohn, Phys. Rev. B **7**, 3541 (1973).

[36] J. E. Inglesfield, Surf. Sci. **188**, L701 (1987).

[37] M. W. Finnis, Surf. Sci. **241**, 61 (1991).

[38] A. L. Boers, Surf. Sci. **63**, 475 (1977).

[39] G. A. Kimmel and B. H. Cooper, Rev. Sci. Instrum. **64**, 672 (1993).

[40] G. A. Kimmel and B. H. Cooper, Phys. Rev. B **48**, 12 164 (1993).

[41] V. E. Yurasova, V. I. Shulga, and D. S. Karpuzov, Can. J. Phys. **46**, 759 (1968).

[42] E. Taglauer and W. Heiland, Surf. Sci. **33**, 27 (1972).

[43] E. S. Parilis and N. Yu. Turaev, Dokl. Akad. Nauk SSSR **10**, 212 (1965) [Sov. Phys. Dokl. **10**, 212 (1965)].

[44] T. C. M. Horn, A. W. Kleyn, and B. Dijkhuis, Chem. Phys. **149**, 275 (1991).

[45] B. Poelsema, L. K. Verhey, and A. L. Boers, Surf. Sci. **56**, 445

(1976); **60**, 485 (1976); **64**, 537 (1977); **64**, 554 (1977).

[46] U. Gerlach-Meyer, E. Hulpke, and H. D. Meyer, Chem. Phys. **36**, 327 (1979).

[47] C. A. Keller, C. A. DiRubio, G. A. Kimmel, and B. H. Cooper, Phys. Rev. Lett. **75**, 1654 (1995).

[48] K. Burke, J. H. Jensen, and W. Kohn, Surf. Sci. **241**, 211 (1991).

[49] J. R. Klein and M. W. Cole, Surf. Sci. **81**, L319 (1979).

[50] A. Hurkmans, E. G. Overbosch, D. R. Olander, and J. Los, Surf. Sci. **54**, 154 (1976).

[51] A. Hurkmans, E. G. Overbosch, and J. Los, Surf. Sci. **59**, 488 (1976).

[52] R. L. Gerlach and T. N. Rhodin, Surf. Sci. **19**, 403 (1970).

[53] K. J. Snowdon, D. J. O'Connor, and R. J. Macdonald, Phys. Rev. Lett. **61**, 1760 (1988).

[54] M. J. Frisch *et al.*, GAUSSIAN 88 (Gaussian, Inc., Pittsburgh, 1988).

[55] *Handbook of Gaussian Basis Sets*, edited by R. Poirier, R. Kari, and I. G. Csizmadia (Elsevier, Amsterdam, 1985).

[56] *Gaussian Basis Sets for Molecular Calculations*, edited by S. Huzinaga (Elsevier, Amsterdam, 1984).

[57] D. Post and E. J. Baerends, J. Chem. Phys. **78**, 5663 (1983).

[58] W. R. Wadt and P. J. Hay, J. Chem. Phys. **82**, 284 (1985); **82**, 299 (1985).